Figure 3. Formation of Ubiquitin- and p62-Positive Inclusions in Autophagy-Deficient Neurons

(A) Accumulation of p62 in *Atg7*-deficient brains. Brain homogenates from *Atg7^{F/F}* and *Atg7^{F/F}*:Nes mice at 8 weeks of age were subjected to SDS-PAGE and analyzed by immunoblotting with indicated antibodies. Data shown are representative of three separate experiments.

(B) Quantitation of p62 mRNA level in *Atg7*-deficient brains by RT-PCR. Total RNAs were prepared from brains of *Atg7^{F/F}* and *Atg7^{F/F}*:Nes mice at 8 weeks of age and analyzed as shown in Figure 2E. Data are mean ± SD values of p62 mRNA normalized to the amount in *Atg7^{F/F}* brain. The experiments were performed three times.

(C) Immunofluorescence microscopy in *Atg7^{F/F}*:Nes cerebral cortex. Brain sections of *Atg7^{F/F}*:Nes mice were immunostained with anti-LC3 and p62 antibodies (left panels) or anti-ubiquitin and p62 antibodies (right panels). Bottom panels show merged images. Bar, 10 μm.

(D) Immunoelectron micrograph showing labeling of p62 (top panel) or double labeling of ubiquitin (10 nm cgp) and p62 (5 nm cgp) in hypothalamic neurons of 8-week-old *Atg7^{F/F}*:Nes mice. Bars, 0.5 μm. Magnified images can be seen in Figure S5.

Loss of p62 Suppresses Inclusion Formation in Autophagy-Deficient Hepatocytes

Next, to investigate the roles of p62 in inclusion formation, we crossed $Atg7^{F/F}$:Mx1 with $p62^{-/-}$ mice, producing the Atg7- and p62-double knockout (DKO) mice ($Atg7^{F/F}$:Mx1:$p62^{-/-}$). In contrast to large number of inclusions positive for ubiquitin in Atg7-deficient hepatocytes, surprisingly such ubiquitin inclusions were almost completely dispersed in the DKO hepatocytes (Figure 4A). Immunoblot analysis revealed that the amounts of accumulated polyubiquitinated proteins in DKO liver were lower than those in Atg7-deficient liver. Moreover, the reduction was more prominent in the insoluble fraction (Figures 4B and S10A). Interestingly, proteasome function evaluated by the degradation of polyubiquitinated protein was not significantly different among the genotypes (Figure S11A). Furthermore, the degradation of long-lived protein in DKO hepatocytes was significantly reduced to the levels as shown in Atg7-deficient hepatocytes (Figure S11C). Electron microscopic analysis showed that the number of aggregate structures and aberrant concentric membranous structures that were typical in Atg7-deficient hepatocytes (Komatsu et al., 2005) were markedly reduced, whereas smooth endoplasmic reticulum and peroxisomes were still abundantly observed in DKO hepatocytes (Figure 4C).

Loss of p62 Suppresses Inclusion Formation in Autophagy-Deficient Neurons

We also examined the roles of p62 in inclusion formation in autophagy-deficient neurons. As shown in Figure S8, while no ubiquitin-positive inclusions were detected in the brains of wild-type and p62-knockout mice, ubiquitin-positive inclusions of various sizes were recognized immunohistochemically in several regions of the $Atg7^{F/F}$:Nes brain. Such inclusions were hardly detected in the $Atg7^{F/F}$:Nes:$p62^{-/-}$ (DKO) neurons (Figures 4D and S8). Unlike autophagy-deficient livers, it was difficult to convincingly detect by immunoblot analyses any differences in the amount of insoluble polyubiquitinated protein between Atg7- and Atg7/p62-DKO brain (Figures 4E and S10B). This discrepancy could be due to the relatively low amounts of insoluble ubiquitinated proteins in total brain lysates from $Atg7^{F/F}$:Nes mice, which were insufficient for the detection of the difference. Actually, the inclusions were observed in some restricted areas such as the hypothalamus and cerebral cortex, and they were hardly observed in glial cells (Hara et al., 2006; Komatsu et al., 2006). Previous electron microscopic analysis showed that the hypothalamic neurons in $Atg7^{F/F}$:Nes brain contained large inclusion bodies in the perikarya (Komatsu et al., 2006). Although such inclusions were hardly detected in the same region of DKO brain, we noticed the presence of several large neuritic structures with numerous pleomorphic features of smooth endoplasmic reticulum (Figure 4F; c, e, and f). Similar alteration was also observed in the $Atg7^{F/F}$:Nes hypothalamus (Figure 4F, b and d), but not in the control (Figure 4F, a). In the cerebellar nuclei of both $Atg7^{F/F}$:Nes and DKO brains, which contained abundant round eosinophilic structures as evident in hematoxylin and eosin (H&E) stained sections (Figure 6C, bottom panel), myelinated axons were frequently enlarged and contained aberrant membranous structures and/or degenerated materials (Figures S12B–S12F), suggesting axonal degeneration in both $Atg7^{F/F}$:Nes and DKO neurons. Taken together, these results strongly suggest that the inclusion formation but not axonal degeneration is largely dependent on the presence of p62 in autophagy-deficient neurons.

Liver Injury in Autophagy-Deficient Mice Is Suppressed by Loss of p62

To examine whether abnormalities in autophagy-deficient liver are partly caused by the accumulation of p62, we examined the phenotypes of $Atg7^{F/F}$:Mx1:$p62^{-/-}$ mice. Surprisingly, simultaneous loss of Atg7 and p62 in the liver significantly suppressed the deleterious phenotypes caused by ablation of autophagy (Figures 5A and 5B). Indeed, histological analysis showed hepatocytic hypertrophy in Atg7-deficient liver and its suppression in DKO liver. Accordingly, the hepatic lobular structure was considerably better recognized in DKO than in Atg7-deficient liver (Figure 5C). While serum levels of aspartate aminotransferase (AST), alanine aminotransferase (ALT), and alkaline phosphatase (ALP) were elevated in the DKO mice compared with the control mice, the levels were markedly lower than those in single Atg7-deficient mice (Figure 5D). Almost the same results were observed in $Atg7^{F/F}$:Alb:$p62^{-/-}$ mice, which exhibited impaired autophagy in hepatocytes at postnatal stage, without pIpC injection (Figure S13), indicating that pIpC injection itself does not affect phenotypes of $Atg7^{F/F}$:Mx1 or $Atg7^{F/F}$:Mx1:$p62^{-/-}$ mice. Taken together, these results indicate that excess accumulation of p62 is a major cause of the pathogenic changes seen in the liver of autophagy-deficient mice.

Ablation of p62 Leads to Neither Improvement nor Exacerbation of the Phenotypes in Autophagy-Deficient Neurons

Further, to investigate whether defects in autophagy-deficient brain are also attributed to accumulation of p62 in neurons, we examined the phenotypes of $Atg7^{F/F}$:Nes:$p62^{-/-}$ mice. In contrast to the recovery of liver injury in $Atg7^{F/F}$:Mx1 mice by simultaneous loss of p62, ablation of p62 did not rescue behavioral abnormalities such as tremor and abnormal limb clasping recognized in $Atg7^{F/F}$:Nes mice (data not shown). Furthermore, histological

(E) Appearance of p62- and ubiquitin-positive inclusions in Atg7-deficient cerebral cortex during postnatal (P) development. $Atg7^{F/F}$:Nes mice were sacrificed at P2, 5, 11, and 28 days, and the brain sections were immunostained with anti-ubiquitin and p62 antibodies. Bottom panels show merged images. Bar, 20 μm.
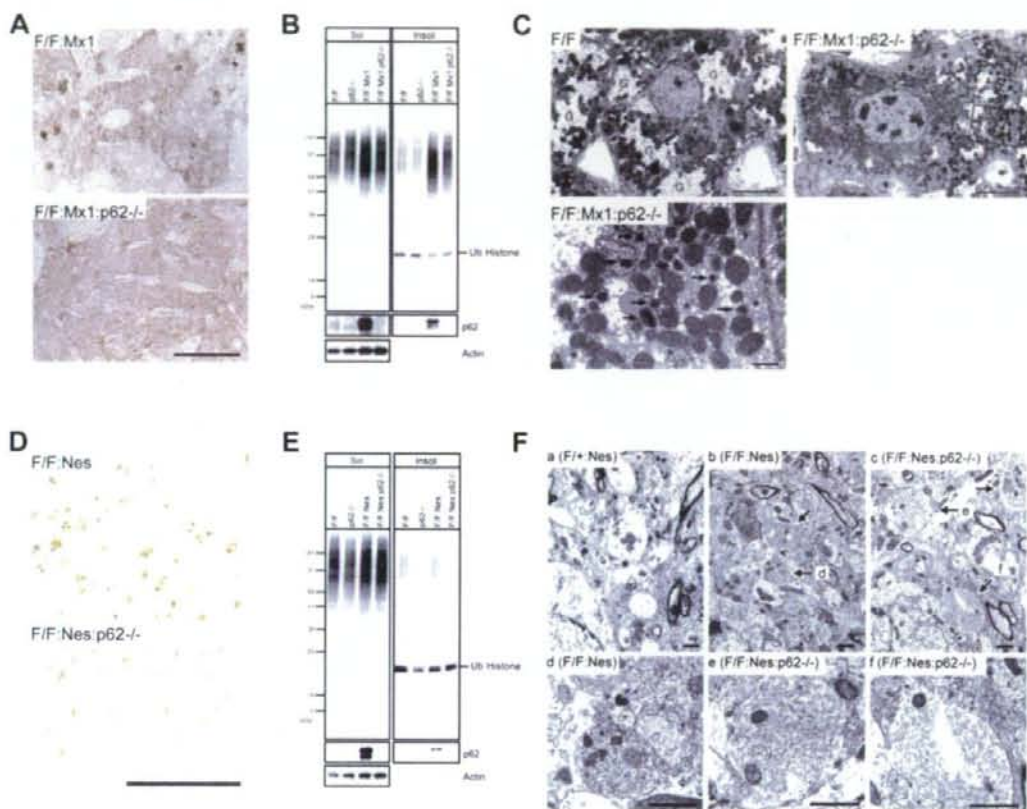
Figure 4. Indispensable Role of p62 in Inclusion Formation in Autophagy-Deficient Cells

(A) Immunohistochemical analysis of ubiquitin inclusions in *Atg7*- and *Atg7/p62*-deficient liver. Liver sections from *Atg7^F/F*:Mx1 and *Atg7^F/F*: Mx1:*p62^−/−* mice at 14-day post-plpC injection were immunostained with anti-ubiquitin antibody. Bar, 100 μm.

(B) Immunoblotting analysis of *Atg7*- and *Atg7/p62*-deficient livers. Liver homogenates from mice of the indicated genotype at 28-day post-plpC injection were separated into detergent-soluble and insoluble fractions as shown in Figure 2. Each fraction was subjected to SDS-PAGE and analyzed by immunoblotting with indicated antibodies. Data shown are representative of three separate experiments.

(C) Electron micrographs of control and *Atg7/p62*-deficient liver. Note that the glycogen area (G), easily observed in control hepatocytes, is markedly reduced in *Atg7/p62*-deficient hepatocytes. The boxed region in the top right panel is further magnified in the bottom left panel. Asterisks indicate regions filled with smooth endoplasmic reticulum. Arrows indicate peroxisomes. Bars, 10 μm (left and right top panels) and 1 μm (left bottom panel).

(D) Immunohistochemical analysis of *Atg7*- and *Atg7/p62*-deficient brains. The presence of ubiquitin-positive particles was examined immunohisto-chemically in the hypothalamic regions of *Atg7^F/F*:Nes and *Atg7^F/F*:Nes:*p62^−/−* mice. Bar, 100 μm.

(E) Immunoblotting analysis of *Atg7*- and *Atg7/p62*-deficient brains. Brain homogenates from mice of the indicated genotypes at 8 weeks of age were analyzed by immunoblotting as shown in (B). Data shown are representative of three separate experiments.

(F) Electron micrographs of the hypothalamus of mice of the indicated genotype. Note that several electron-lucent neuritic structures are detected in the control neuropil (a), which are only rarely seen in the *Atg7*- (b) and *Atg7/p62*-deficient (c) tissues. Instead, the latter tissues contain large neurites filled with pleomorphic features of smooth endoplasmic reticulum. Arrows indicate abnormal neuritic structures, some of which are magnified in d, e, and f. Bars, 1 μm.

analyses clearly revealed the lack of Purkinje cells in the cerebellum (Figure 6C) and large pyramidal neurons in both the cerebral cortex (Figure 6A) and hippocampus (Figure 6B) of *Atg7^F/F*:Nes:*p62^−/−* as well as *Atg7^F/F*:Nes mice. We also found a number of eosinophilic spheroids in H&E-stained sections in the cerebellar nuclei of *Atg7^F/F*: Nes:*p62^−/−* mice, similar to *Atg7^F/F*:Nes mice (Figure 6C). A marked increase in the number of TUNEL (terminal deox-

ynucleotidyl transferase [TdT]-mediated dUTP-biotin nick end labeling)-positive cells, which were noted in both *Atg7^F/F*:Nes cerebral cortices and granular cell layers of the cerebellum at P28, tended to decrease in similar regions of *Atg7^F/F*:Nes:*p62^−/−* mice (Figures 6D and 6E), albeit sta-tistically insignificant. Thus, these results indicate that abla-tion of *p62* does not result in improvement or exacerbation of the phenotypes in autophagy-deficient neurons.
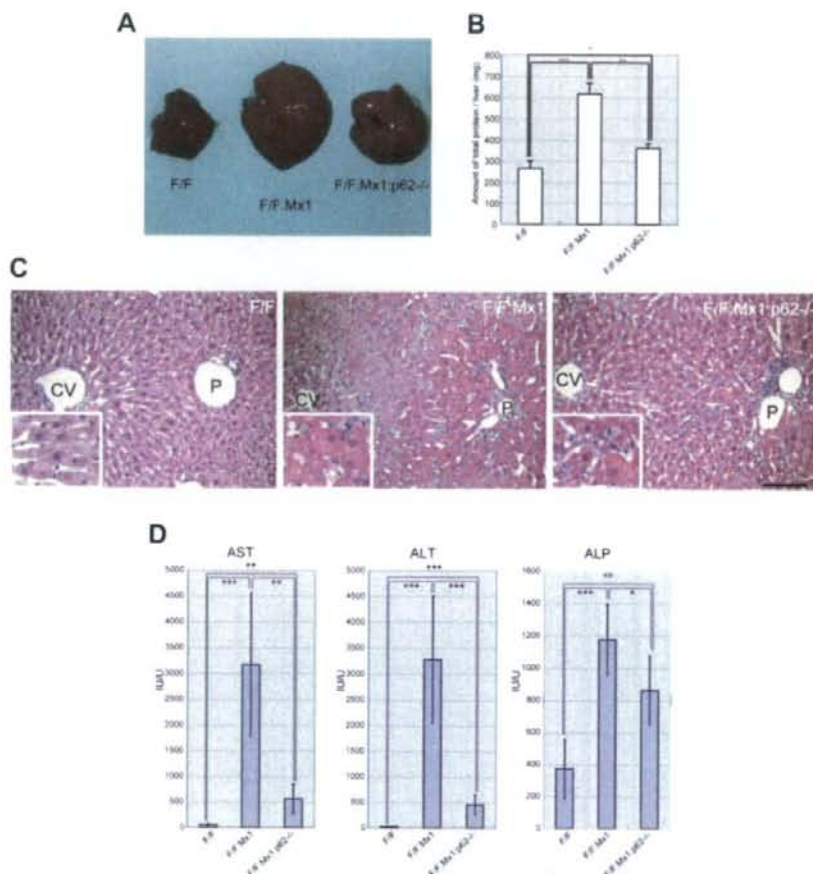
Figure 5. Suppression of Liver Dysfunction in Autophagy-Deficient Mice by Additional Loss of *p62*

(A) Gross anatomical views of representative livers from mice of the indicated genotype at 28-day post-plpC injection.

(B) Amount of total liver protein. Livers from mice shown in (A) were dissected out, and amounts of total protein per liver were measured. Data are mean ± SD values of five mice in each group. $^*p < 0.05$, $^{**}p < 0.01$, and $^{***}p < 0.001$ (Student's t test).

(C) Typical histology of livers from mice of the indicated genotype. H&E staining of respective livers was conducted at 56-day post-plpC injection. Higher magnification views are shown in insets. CV, central vein; P, portal vein. Bar, 100 μm.

(D) Liver function tests of mice shown in (A). Serum levels of AST, ALT, and ALP were measured. Data represent mean ± SD values of seven mice in each group. $^*p < 0.05$, $^{**}p < 0.01$, and $^{***}p < 0.001$.

Aberrant Accumulation of p62 Induces Detoxifying Enzymes in Livers but Not in Brains

Our data clearly showed that loss of *p62* suppresses liver dysfunction but not neurodegeneration in autophagy-deficient mice. How does p62 function differently in autophagy-deficient liver and brain? To elucidate the underlying mechanism for the difference, we examined gene-expression profiles in autophagy-deficient mice by microarray analyses and found that detoxifying enzymes including glutathione S-transferase (GST) families, cytochrome P450 families, and NAD(P)H dehydrogenase quinone 1 (Nqo1) were highly expressed in the autophagy-deficient liver. However, none of these detoxifying enzymes was upregulated in the autophagy-deficient brain (Figure 7A). Moreover, such induction in the liver was suppressed almost completely by additional loss of *p62* (Figure 7A). As shown in Figure 2D, accumulation and insolubilization of both p62 and ubiquitinated proteins began at 4 days post-plpC injection in *Atg7^{F/F}*:Mx1 liver. Furthermore, upregulation of detoxifying enzymes began at 8 days and reached a plateau at 12 days post-plpC injection (Figure 7B). Meanwhile, significant leakage of ALT and AST, representing hepatocyte death, occurred at later time points (Figure 7C), suggesting that the increase of detoxifying enzymes was not a secondary effect of liver dysfunction.
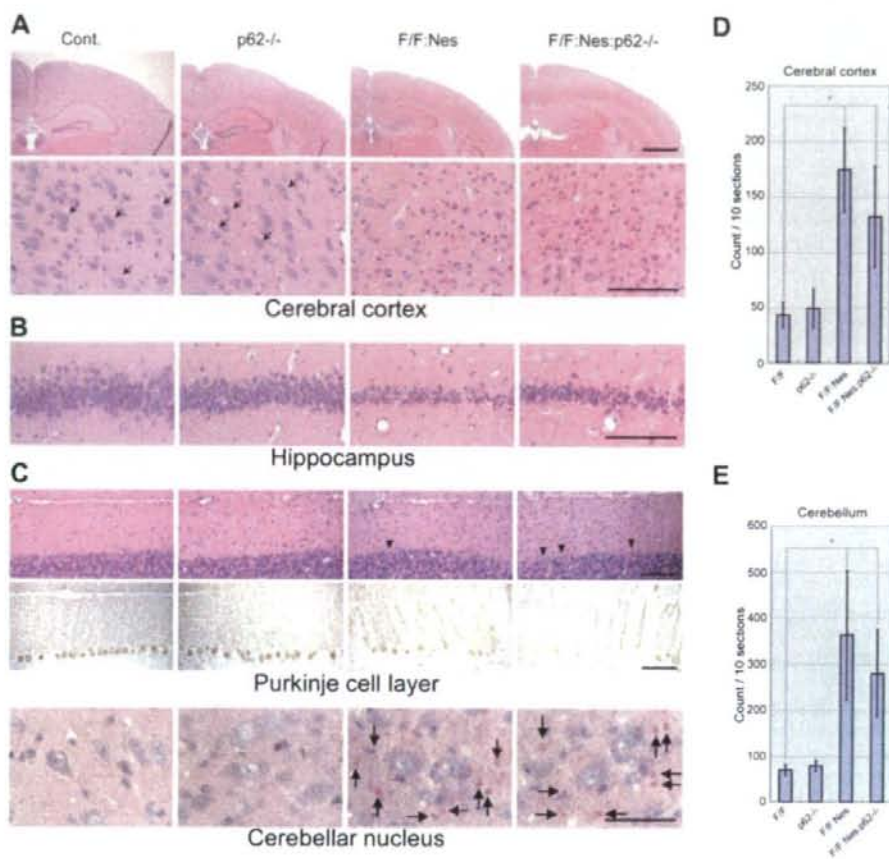
Figure 6. Ablation of *p62* Leads to Neither Improvement nor Exacerbation of the Phenotypes in Autophagy-Deficient Neurons

(A and B) H&E staining of the cerebral cortex (A) and pyramidal cell layer of the hippocampus (B) in mice of the indicated genotype at 4 weeks of age. Top panels in (A) are magnified in bottom panels. Arrows in (A) point to large pyramidal neurons in the cerebral cortex.

(C) Histological analysis of the cerebellar cortex (top and middle panels) and cerebellar nucleus (bottom panel). Cryosections from 8-week-old mice were stained with H&E (top and bottom panels) or immunostained with Purkinje cell marker, calbindin (middle panels). Bars, 1 mm (A, top panel), 200 μm (C, bottom panel), 100 μm (A, bottom panel), (B and C, top and middle panels).

(D and E) Apoptotic cells in the cerebral cortex (D) and cerebellum (E) at 8 weeks of age of the indicated four genotypes. Bars represent the average number (±SD) of total TUNEL-positive cells in ten sections counted in three animals for each genotype. *p < 0.05.

A key question is how such enzymes are specifically induced in the autophagy-deficient liver. To this end, we examined the behavior of the transcriptional factor "Nrf2," which translocates to the nucleus in response to oxidative and electrophilic stresses to activate the transcription of various detoxifying enzymes including Gstm1 and Nqo1 (Tong et al., 2006). As shown in Figure 7D, the level of Nrf2 was markedly higher in the nuclear fraction from *Atg7^{F/F}*:Mx1 liver but very low in those from control and *p62*-knockout livers. Importantly, the translocation of Nrf2 into the nucleus in *Atg7^{F/F}*:Mx1 liver was almost completely suppressed by additional loss of *p62*, implying that autophagy-deficiency causes cellular stress in the liver, which negatively affects hepa-

tocyte function and concomitantly induces p62-dependent activation of Nrf2.

DISCUSSION

p62 Handles Formation of Cytoplasmic Inclusions

While there is ample evidence that dysfunction of the ubiquitin-proteasome system leads to the formation of ubiquitin-positive inclusions, which are the pathological hallmark of various neurodegenerative diseases (Goldberg, 2003), suppression of autophagy also leads to the formation of ubiquitin-positive inclusion (Hara et al., 2006; Komatsu et al., 2005, 2006). However, the molecular mechanism(s) involved in the formation of these inclusions is not clear to

date. In the present study, we found marked accumulation of p62 and ubiquitinated proteins and subsequent inclusion formation in *Atg7*-deficient mice (Figures 2 and 3). Intriguingly, p62 has been identified as a major component of ubiquitin-containing inclusions known as the "hepatocytic Mallory body" found in alcoholic hepatitis and steatohepatitis (Stumptner et al., 2002). Similar inclusions have been also recognized frequently in proteinaceous aggregates in the remnant neurons in various neurodegenerative disorders such as Parkinson's disease and amyotrophic lateral sclerosis (Kuusisto et al., 2001; Nakano et al., 2004). In such diseases, it is plausible that the reduced autophagic activity may be associated with the generation of inclusion bodies.

Surprisingly, loss of *p62* was associated with marked reduction of ubiquitin-positive inclusions, which were otherwise abundantly present in *Atg7*-deficient hepatocytes and neurons (Figure 4). Because ubiquitin-tagged proteins are sticky but do not exhibit aggregation-prone nature themselves, the high levels of p62 due to impaired autophagy might predispose to inclusion formation via the PB1 domain, which retains the ability of self oligomerization (Lamark et al., 2003). Indeed, overexpression of p62 forms inclusions, which is dependent on the presence of both PB1 and UBA domains (Bjorkoy et al., 2005). Since almost all inclusions in autophagy-deficient cells were positive for both ubiquitin and p62, it is possible that ubiquitinated proteins initially interact with p62, and subsequently the protein complex becomes inclusions in a p62-dependent manner. Although autophagy is involved in protection from several discrete diseases (Fortun et al., 2003; Kamimoto et al., 2006; Ravikumar et al., 2004), whether p62 is indeed essential for the formation of disease-related inclusions or not remains unknown at present. However, intriguingly, the formation of ubiquitin-positive aggregates induced by proteasome inhibition is greatly suppressed in *p62*-deficient cells (Wooten et al., 2006), suggesting that p62 is a general mediator of inclusion formation.

p62-Dependent Liver Impairment in Autophagy-Deficient Mice

Our present studies suggest that the pathological changes in *Atg7*-deficient liver are due, at least in part, to oxidative stress associated with proteinaceous aggregates formed by excess accumulation of p62 and ubiquitinated proteins. However, emerging evidence indicates that protein aggregates containing disease-related proteins (e.g., polyQ) can provide protection (Arrasate et al., 2004; Ross and Poirier, 2005; Sanchez et al., 2003). Similarly, aggregate formation mediated by p62 seems to be a protective mechanism in the presence of overexpression of polyQ (Bjorkoy et al., 2005). Therefore, p62 might play an important role in the surveillance of protein abnormalities by adaptively segregating ubiquitin-tagged toxic proteins as inclusions in cells. It is noteworthy that oligomer and protofibrillar intermediates, which are cytotoxic (Arrasate et al., 2004; Ross and Poirier, 2005; Sanchez et al., 2003), must form before

the formation of harmless aggregates and generate reactive oxygen species, which are the primary mediators of oxidative stress (Tabner et al., 2005). Because genetic ablation of autophagy in the liver causes exhaustive accumulation of both p62 and ubiquitinated proteins, the liver might show mixed symptoms related to the cytotoxic effects and protective reactions—i.e., continuous formation of both "harmful oligomer and protofibrillar intermediates" and "harmless aggregates" and induction of both "oxidative stress" and "detoxifying enzymes." According to this scenario, simultaneous loss of p62 under autophagy-deficient background might attenuate accumulation of unfavorable harmful oligomer and protofibrillar intermediates, which ultimately form harmless inclusion, leading to alleviation of liver injury.

In this context, we found that impairment of liver autophagy led to nuclear translocation of Nrf2 (Figure 7D), which is responsible for inducible transcription of various antioxidant and detoxifying enzymes, providing mechanistic insights into the upregulation of those enzymes in the autophagy-deficient liver. In the absence of stress, Nrf2 is constitutively degraded through the ubiquitin-proteasome pathway, since the binding partner Keap1 is a ubiquitin-protein ligase. Exposure to oxidative and electrophilic insults results in modification of Cys residues of Keap1, and leads to inactivation of Keap1. Stabilization of Nrf2 leads to its nuclear translocation to induce the transcription of detoxifying enzymes (Tong et al., 2006). Accordingly, we surmise that the autophagy-deficient liver may be filled with oxidative and/or other Nrf2-inducing stresses. More interestingly, simultaneous loss of *p62* and *Atg7* completely suppressed the translocation of Nrf2 (Figure 7D). These results strongly argue for accumulation of cellular stress in autophagy-deficient liver, the extent of which depends on the impairment of p62 turnover, and they shed light on the mechanism of p62 loss-associated attenuation of autophagy-deficiency-related liver injury.

On the other hand, leakage of hepatocytic enzymes into peripheral blood still occurred at a significantly high level in *Atg7^{F/F}*:Mx1:*p62^{-/-}* compared with control mice (Figure 5D), implying other abnormalities apart from p62 accumulation in the DKO livers. In fact, in addition to accumulation of soluble ubiquitinated proteins, impairment of organelle turnover was not rescued by the additional defect of *p62* (Figures 4B and 4C). Such abnormalities together with the excess accumulation of p62 might have irreversible cytotoxic effects in autophagy-deficient hepatocytes.

p62-Independent Neuronal Death in Autophagy-Deficient Mice

Unlike the liver, the survival of *Atg7*-deficient neurons is affected little when *p62* is abolished, although p62 can form protein aggregates in neuronal cells as in hepatocytes. This paradoxical observation may underlie the difference in autophagic activity among cell-types or tissues. The constitutive autophagic activity in the brain is low compared
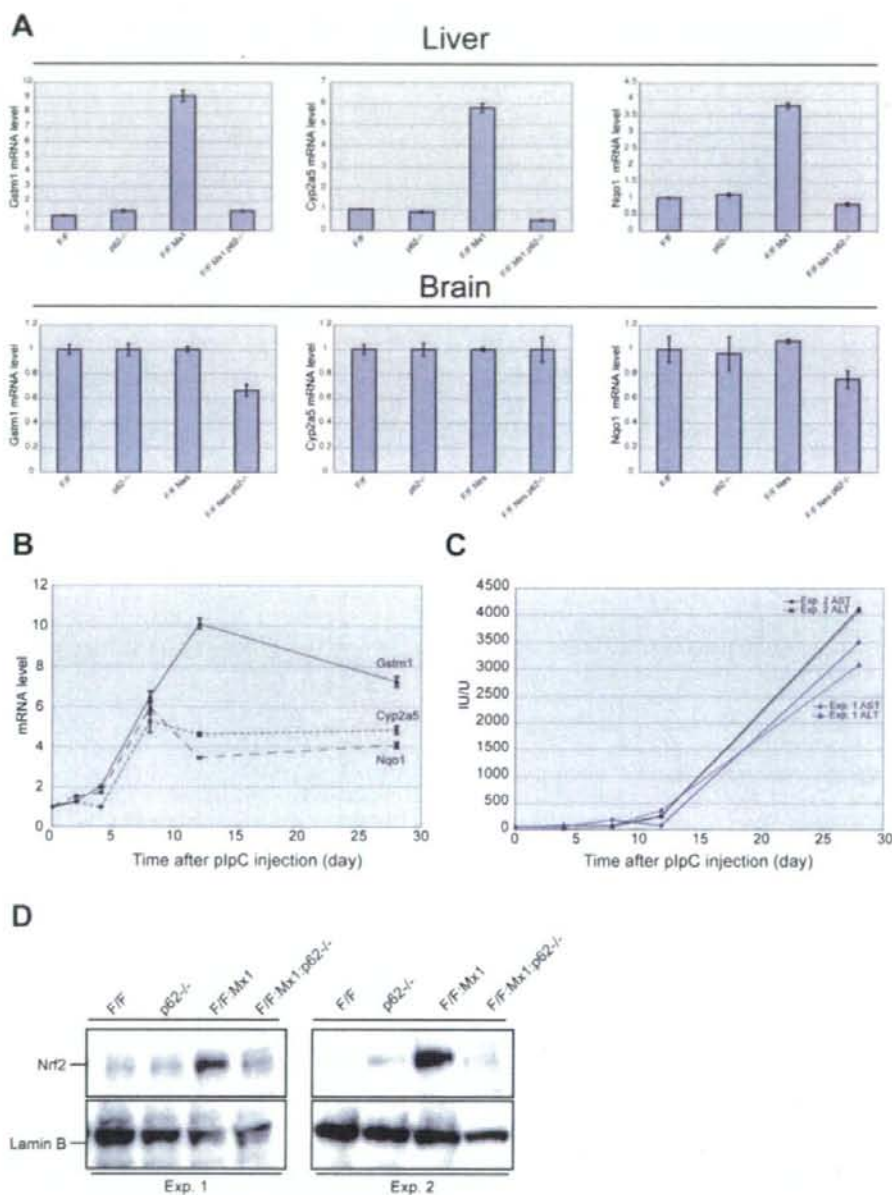
A

Liver

Brain

B

C

D

Exp. 1   Exp. 2

Figure 7. p62-Dependent Induction of Detoxifying Enzymes in Autophagy-Deficient Liver but Not in Brain

(A) Quantitative RT-PCR analyses of Gstm1, Cy2a5, and Nqo1 in mouse liver (top panels) and brain (bottom panels). Total RNAs were prepared from the livers of the indicated genotypes at 12 days post-pIpC injection and brains of the indicated genotypes at postnatal day 28. The values are normalized to the amount of mRNA in $Atg7^{F/F}$ liver and brain. The experiments were performed three times.

(B) Quantitation of mRNA levels of detoxifying enzymes in $Atg7^{F/F}$:Mx1 liver by RT-PCR. Total RNAs were prepared from $Atg7^{F/F}$:Mx1 mice livers at various time points post-pIpC injection, and then cDNA was synthesized from each RNA, followed by real-time PCR analyses. The values are normalized to the amount of each mRNA in $Atg7^{F/F}$:Mx1 liver at 0 days post-pIpC injection.

(C) Liver function tests of mice at various time points post-pIpC injection. Serum levels of AST and ALT were measured in $Atg7^{F/F}$:Mx1 mice. Data represent two independent mice.

with other tissues such as the liver (Mizushima et al., 2004). Accordingly, significant accumulation of ubiquitinated proteins was noted in Atg7-deficient brain, but their levels, especially insoluble ubiquitinated proteins, were lower than in Atg7-deficient liver (Figures 4E and S10B), and severe formation of the inclusion was found in restricted groups of neurons (Figures 4D and S8). Moreover, unlike in the liver, detoxifying enzymes did not increase in Atg7-deficient brain (Figure 7A), suggesting the low susceptibility of neurons to toxicity associated with aggregate formation. In fact, several ubiquitin-positive aggregates were recognized in Atg7-deficient brain regions in the presence of mild neuronal loss (Komatsu et al., 2006).

Why do autophagy-deficient mice develop neurodegeneration? Analyses of Purkinje cell-specific Atg7-knockout mice demonstrated that Atg7-deficient Purkinje cells initially causes cell-autonomous, progressive dystrophy (manifested by axonal swelling) and degeneration of the axon terminals followed by cell-autonomous Purkinje cell death and mouse behavioral deficits (Komatsu et al., 2007). The mutant Purkinje cells developed aberrant organelles in the swelling axons, suggesting the important role of autophagy in the regulation of local axonal membrane trafficking and turnover, and implicate impairment of axonal autophagy as a mechanism for axonopathy associated with neurodegeneration. Importantly, such axonopathy in Atg7-deficient Purkinje cells and hypothalamic neurons was still observed in Atg7/p62-DKO neurons (Figures 4F, 6C, and S12), indicating that the development of axonopathy in Atg7-deficient neurons is p62 independent. Therefore, we hypothesize that the mechanism of neurodegeneration caused by autophagy deficiency might involve distinct pathogenic pathways, such as axonal dystrophy and degeneration.

EXPERIMENTAL PROCEDURES

Generation of Knockout Mice

Atg7$^{F/F}$:Mx1 mice (Komatsu et al., 2005) were bred with GFP-LC3 Tg mice (Mizushima et al., 2004) to generate Atg7$^{F/F}$:Mx1:GFP-LC3 mice. p62$^{-/-}$ mice were bred with Atg7$^{F/F}$:Mx1, Atg7$^{F/F}$:Mx1:GFP-LC3, and Atg7$^{F/F}$:Nes mice (Komatsu et al., 2006) to generate Atg7$^{F/F}$:Mx1:p62$^{-/-}$, Atg7$^{F/F}$:Mx1:p62$^{-/-}$:GFP-LC3, and Atg7$^{F/F}$:Nes:p62$^{-/-}$ mice, respectively. With regard to deletion of Atg7 from the liver, Cre expression in the liver was induced by intraperitoneal injection of pIpC (Sigma Chemical Co., St. Louis, MO) (Komatsu et al., 2005). Mice were housed in specific-pathogen-free facilities, and the experimental protocol was approved by the Ethics Review Committee for Animal Experimentation of Tokyo Metropolitan Institute of Medical Science. Other mice strains shown in Supplemental Data are described in Supplemental Experimental Procedures.

Immunological Analysis

Livers and brains were homogenized in 0.25 M sucrose, 10 mM 2-[4-(2-hydroxyethyl)-1-piperazinyl]ethanesulfonic acid [HEPES], pH 7.4, and 1 mM dithiothreitol (DTT). The resultant homogenates were fractionated into 0.5% Tx-100 soluble and insoluble fractions. Immunoprecipitation and immunoblot analyses were conducted as described previously (Komatsu et al., 2004). Nuclear fraction from the liver was prepared according to the method of Blobel and Potter (Blobel and Potter, 1966). The antibodies for p62, Atg7, and LC3 were described previously (Ishii et al., 1996; Komatsu et al., 2005). The antibodies for GFP (Medical and Biological Laboratories [MBL] Co., Nagoya, Japan), ubiquitin (FK2: MBL), Nrf2 (H-300: Santa Cruz Biotechnology, Inc., Santa Cruz, CA), LDH (ab2101: abcam, Inc., Cambridge, MA), actin (MAB1501R: Chemicon International, Inc., Temecula, CA) and Lamin B (M-20: Santa Cruz Biotechnology, Inc.) were purchased.

Pull-Down Assay

Recombinant GST, GST-LC3, and GST-p62 were produced in Escherichia coli, and recombinant proteins were purified by chromatography on glutathione-Sepharose 4B (Amersham Biosciences, Arlington Heights, IL). The GST-p62 cleaved the GST tag by precision protease (Amersham Biosciences). Purified p62 and GST or GST-LC3 were mixed in TNE buffer (Komatsu et al., 2004) for 3 hr at 4°C and then precipitated with glutathione-Sepharose. The mixtures were washed five times with ice-cold TNE. The bound proteins were analyzed by SDS-PAGE followed by Coomassie brilliant blue (CBB) staining.

Quantitative RT–PCR

cDNA was synthesized from 1 μg of total RNA using the Transcriptor First Strand cDNA Synthesis Kit (Roche Applied Science), and quantitative PCR was performed using LightCycler 480 Probes Masterin (Roche Applied Science) in a LightCycler 480 (Roche Applied Science). Signals were normalized to β-glucronidase (GUS). Primer sequences are described in Supplemental Experimental Procedures.

Immunofluorescence Microscopy of Cultured Hepatocytes

Hepatocytes grown on glass coverslips were immunostained with anti-p62 or ubiquitin (DakoCytomation, Glostrup, Denmark) antibody as described previously (Komatsu et al., 2005). The coverslips were mounted and viewed with a laser-scanning confocal microscope (FV1000, Olympus) or conventional epifluorescent microscope.

Histological Examination

Methods for tissue fixation and subsequent procedures, including H&E staining, immunohistochemistry, conventional electron microscopy, immunoelectron microscopy, and TUNEL staining were described previously (Komatsu et al., 2005, 2006). Antibodies used for immunohistochemistry and immunoelectron microscopy were as follows: rabbit polyclonal antibodies against LC3 (Komatsu et al., 2005), p62 (Ishii et al., 1996), and GFP (Abcam), and mouse monoclonal antibodies against ubiquitin (FK2 and 1B3: MBL).

Statistical Analysis

Data were analyzed by two-tailed Student's t test. For all graphs, data are represented as mean ± SD.

Supplemental Data

Supplemental Data include 13 figures, 1 table, Supplemental Experimental Procedures, and Supplemental References and can be found with this article online at http://www.cell.com/cgi/content/full/131/6/1149/DC1/.

(D) The level of Nrf2 in liver nuclear fraction. Nuclear fractions were prepared from liver of the indicated genotypes at 12 days post-pIpC injection, subjected to SDS-PAGE, and analyzed by immunoblotting with antibodies against Nrf2 and Lamin B (as a control). Data represent two independent mice.

REFERENCES

Arrasate, M., Mitra, S., Schweitzer, E.S., Segal, M.R., and Finkbeiner, S. (2004). Inclusion body formation reduces levels of mutant huntingtin and the risk of neuronal death. Nature *431*, 805–810.

Bjorkoy, G., Lamark, T., Brech, A., Outzen, H., Perander, M., Overvatn, A., Stenmark, H., and Johansen, T. (2005). p62/SQSTM1 forms protein aggregates degraded by autophagy and has a protective effect on huntingtin-induced cell death. J. Cell Biol. *171*, 603–614.

Blobel, G., and Potter, V.R. (1966). Nuclei from rat liver: isolation method that combines purity with high yield. Science *154*, 1662–1665.

Elmore, S.P., Qian, T., Grissom, S.F., and Lemasters, J.J. (2001). The mitochondrial permeability transition initiates autophagy in rat hepatocytes. FASEB J. *15*, 2286–2287.

Fortun, J., Dunn, W.A., Jr., Joy, S., Li, J., and Notterpek, L. (2003). Emerging role for autophagy in the removal of aggresomes in Schwann cells. J. Neurosci. *23*, 10672–10680.

Goldberg, A.L. (2003). Protein degradation and protection against misfolded or damaged proteins. Nature *426*, 895–899.

Hara, T., Nakamura, K., Matsui, M., Yamamoto, A., Nakahara, Y., Suzuki-Migishima, R., Yokoyama, M., Mishima, K., Saito, I., Okano, H., and Mizushima, N. (2006). Suppression of basal autophagy in neural cells causes neurodegenerative disease in mice. Nature *441*, 885–889.

Ichimura, Y., Kirisako, T., Takao, T., Satomi, Y., Shimonishi, Y., Ishihara, N., Mizushima, N., Tanida, I., Kominami, E., Ohsumi, M., et al. (2000). A ubiquitin-like system mediates protein lipidation. Nature *408*, 488–492.

Ishii, T., Yanagawa, T., Kawane, T., Yuki, K., Seita, J., Yoshida, H., and Bannai, S. (1996). Murine peritoneal macrophages induce a novel 60-kDa protein with structural similarity to a tyrosine kinase p56lck-associated protein in response to oxidative stress. Biochem. Biophys. Res. Commun. *226*, 456–460.

Iwata, J., Ezaki, J., Komatsu, M., Yokota, S., Ueno, T., Tanida, I., Chiba, T., Tanaka, K., and Kominami, E. (2006). Excess peroxisomes are degraded by autophagic machinery in mammals. J. Biol. Chem. *281*, 4035–4041.

Kabeya, Y., Mizushima, N., Ueno, T., Yamamoto, A., Kirisako, T., Noda, T., Kominami, E., Ohsumi, Y., and Yoshimori, T. (2000). LC3, a mammalian homologue of yeast Apg8p, is localized in autophagosome membranes after processing. EMBO J. *19*, 5720–5728.

Kamimoto, T., Shoji, S., Hidvegi, T., Mizushima, N., Umebayashi, K., Perlmutter, D.H., and Yoshimori, T. (2006). Intracellular inclusions containing mutant alpha1-antitrypsin Z are propagated in the absence of autophagic activity. J. Biol. Chem. *281*, 4467–4476.

Komatsu, M., Chiba, T., Tatsumi, K., Iemura, S., Tanida, I., Okazaki, N., Ueno, T., Kominami, E., Natsume, T., and Tanaka, K. (2004). A novel protein-conjugating system for Ufm1, a ubiquitin-fold modifier. EMBO J. *23*, 1977–1986.

Komatsu, M., Waguri, S., Ueno, T., Iwata, J., Murata, S., Tanida, I., Ezaki, J., Mizushima, N., Ohsumi, Y., Uchiyama, Y., et al. (2005). Impairment of starvation-induced and constitutive autophagy in Atg7-deficient mice. J. Cell Biol. *169*, 425–434.

Komatsu, M., Waguri, S., Chiba, T., Murata, S., Iwata, J., Tanida, I., Ueno, T., Koike, M., Uchiyama, Y., Kominami, E., and Tanaka, K. (2006). Loss of autophagy in the central nervous system causes neurodegeneration in mice. Nature *441*, 880–884.

Komatsu, M., Wang, Q.J., Holstein, G.R., Friedrich, V.L., Iwata, J.I., Kominami, E., Chait, B.T., Tanaka, K., and Yue, Z. (2007). Essential role for autophagy protein Atg7 in the maintenance of axonal homeostasis and the prevention of axonal degeneration. Proc. Natl. Acad. Sci. USA *104*, 14489–14494.

Kuma, A., Hatano, M., Matsui, M., Yamamoto, A., Nakaya, H., Yoshimori, T., Ohsumi, Y., Tokuhisa, T., and Mizushima, N. (2004). The role of autophagy during the early neonatal starvation period. Nature *432*, 1032–1036.

Kuusisto, E., Salminen, A., and Alafuzoff, I. (2001). Ubiquitin-binding protein p62 is present in neuronal and glial inclusions in human tauopathies and synucleinopathies. Neuroreport *12*, 2085–2090.

Lamark, T., Perander, M., Outzen, H., Kristiansen, K., Overvatn, A., Michaelsen, E., Bjorkoy, G., and Johansen, T. (2003). Interaction codes within the family of mammalian Phox and Bem1p domain-containing proteins. J. Biol. Chem. *278*, 34568–34581.

Levine, B., and Klionsky, D.J. (2004). Development by self-digestion: molecular mechanisms and biological functions of autophagy. Dev. Cell *6*, 463–477.

Mizushima, N., Yamamoto, A., Hatano, M., Kobayashi, Y., Kabeya, Y., Suzuki, K., Tokuhisa, T., Ohsumi, Y., and Yoshimori, T. (2001). Dissection of autophagosome formation using Apg5-deficient mouse embryonic stem cells. J. Cell Biol. *152*, 657–668.

Mizushima, N., Yamamoto, A., Matsui, M., Yoshimori, T., and Ohsumi, Y. (2004). In vivo analysis of autophagy in response to nutrient starvation using transgenic mice expressing a fluorescent autophagosome marker. Mol. Biol. Cell *15*, 1101–1111.

Moscat, J., Diaz-Meco, M.T., Albert, A., and Campuzano, S. (2006). Cell signaling and function organized by PB1 domain interactions. Mol. Cell *23*, 631–640.

Nakano, T., Nakaso, K., Nakashima, K., and Ohama, E. (2004). Expression of ubiquitin-binding protein p62 in ubiquitin-immunoreactive intraneuronal inclusions in amyotrophic lateral sclerosis with dementia: analysis of five autopsy cases with broad clinicopathological spectrum. Acta Neuropathol. (Berl.) *107*, 359–364.

Ohsumi, Y. (2001). Molecular dissection of autophagy: two ubiquitin-like systems. Nat. Rev. Mol. Cell Biol. *2*, 211–216.

Ravikumar, B., Vacher, C., Berger, Z., Davies, J.E., Luo, S., Oroz, L.G., Scaravilli, F., Easton, D.F., Duden, R., O'Kane, C.J., and Rubinsztein, D.C. (2004). Inhibition of mTOR induces autophagy and reduces toxicity of polyglutamine expansions in fly and mouse models of Huntington disease. Nat. Genet. *36*, 585–595.

Rodriguez, A., Duran, A., Selloum, M., Champy, M.F., Diez-Guerra, F.J., Flores, J.M., Serrano, M., Auwerx, J., Diaz-Meco, M.T., and Moscat, J. (2006). Mature-onset obesity and insulin resistance in mice deficient in the signaling adapter p62. Cell Metab. *3*, 211–222.

Ross, C.A., and Poirier, M.A. (2005). Opinion: What is the role of protein aggregation in neurodegeneration? Nat. Rev. Mol. Cell Biol. *6*, 891–898.

Sanchez, P., De Carcer, G., Sandoval, I.V., Moscat, J., and Diaz-Meco, M.T. (1998). Localization of atypical protein kinase C isoforms into lysosome-targeted endosomes through interaction with p62. Mol. Cell. Biol. *18*, 3069–3080.

Sanchez, I., Mahlke, C., and Yuan, J. (2003). Pivotal role of oligomerization in expanded polyglutamine neurodegenerative disorders. Nature *421*, 373–379.

Stumptner, C., Fuchsbichler, A., Heid, H., Zatloukal, K., and Denk, H. (2002). Mallory body–a disease-associated type of sequestosome. Hepatology *35*, 1053–1062.

Tabner, B.J., El-Agnaf, O.M., German, M.J., Fullwood, N.J., and Allsop, D. (2005). Protein aggregation, metals and oxidative stress in neurodegenerative diseases. Biochem. Soc. Trans. *33*, 1082–1086.

Tong, K.I., Kobayashi, A., Katsuoka, F., and Yamamoto, M. (2006). Two-site substrate recognition model for the Keap1-Nrf2 system: a hinge and latch mechanism. Biol. Chem. *387*, 1311–1320.

Tsukada, M., and Ohsumi, Y. (1993). Isolation and characterization of autophagy-defective mutants of Saccharomyces cerevisiae. FEBS Lett. *333*, 169–174.

Wang, Q.J., Ding, Y., Kohtz, D.S., Mizushima, N., Cristea, I.M., Rout, M.P., Chait, B.T., Zhong, Y., Heintz, N., and Yue, Z. (2006). Induction of autophagy in axonal dystrophy and degeneration. J. Neurosci. *26*, 8057–8068.

Wooten, M.W., Hu, X., Babu, J.R., Seibenhener, M.L, Geetha, T., Paine, M.G., and Wooten, M.C. (2006). Signaling, polyubiquitination, trafficking, and inclusions: Sequestosome 1/p62's role in neurodegenerative disease. J. Biomed. Biotechnol. *2006*, 62079.

LETTERS

Toll-like receptor signalling in macrophages links the autophagy pathway to phagocytosis

Miguel A. Sanjuan[1], Christopher P. Dillon[1], Stephen W. G. Tait[1], Simon Moshiach[2], Frank Dorsey[3], Samuel Connell[1], Masaaki Komatsu[4], Keiji Tanaka[4], John L. Cleveland[5], Sebo Withoff[1] & Douglas R. Green[1]

Phagocytosis and autophagy are two ancient, highly conserved processes involved, respectively, in the removal of extracellular organisms and the destruction of organisms in the cytosol[1–3]. Autophagy, for either metabolic regulation or defence, involves the formation of a double membrane called the autophagosome, which then fuses with lysosomes to degrade the contents[4], a process that has similarities with phagosome maturation. Toll-like-receptor (TLR) engagement activates a variety of defence mechanisms within phagocytes[5], including facilitation of phagosome maturation[6], and also engages autophagy[7]. Therefore we speculated that TLR signalling might link these processes to enhance the function of conventional phagosomes. Here we show that a particle that engages TLRs on a murine macrophage while it is phagocytosed triggers the autophagosome marker LC3 to be rapidly recruited to the phagosome in a manner that depends on the autophagy pathway proteins ATG5 and ATG7; this process is preceded by recruitment of beclin 1 and phosphoinositide-3-OH kinase activity. Translocation of beclin 1 and LC3 to the phagosome was not associated with observable double-membrane structures characteristic of conventional autophagosomes, but was associated with phagosome fusion with lysosomes, leading to rapid acidification and enhanced killing of the ingested organism.

A critical step in the autophagy process is the ligation of LC3 to phosphatidylethanolamine, resulting in aggregates of LC3[8]. In order to visualize processes related to autophagy, we used green fluorescent protein (GFP)–LC3[9] in the RAW macrophage cell line (RAW-GFP–LC3). As shown previously for lipopolysaccharide (LPS)[7], on stimulation of TLRs with LPS, CpG, or imiquimod for several hours, we observed the formation of LC3 aggregates (Supplementary Fig. 1a; quantification is shown in Supplementary Fig. 1b) and the generation of the conjugated form of LC3 (Supplementary Fig. 1c). We then examined the effects of TLR engagement on LC3 localization during phagocytosis. Latex beads with or without the associated TLR ligand PAM3CSK4 were fed to RAW-GFP–LC3 cells (Fig. 1a). The presence of the TLR agonist induced a rapid recruitment of LC3 to the phagosome, which was not seen in the absence of the agonist. Similar effects were observed on ingestion of beads with LPS (Fig. 1a), killed yeast (zymosan) (Fig. 1b, time course shown in Supplementary Fig. 2a) or *Escherichia coli* bacteria (Supplementary Fig. 3a, 3b, and Supplementary Movie 1). Internalization of particles was confirmed after each experiment by visual microscopic inspection (Supplementary Fig. 2b). Time lapse analysis of the recruitment of GFP–LC3 to phagosomes (Fig. 1c and Supplementary Movie 2) revealed that this process occurred rapidly (≤15 min after internalization) and was transient, with the effect waning after approximately 60 min.

Zymosan is recognized by TLR2 (ref. 10) and therefore we used mice deficient in this receptor[11] to test the role of TLR in LC3 recruitment to the phagosome. Primary macrophages from $Tlr2^{-/-}$ mice showed a reduced translocation of LC3 in response to zymosan (Fig. 1d, quantified in Fig. 1e). This was consistent with the reduced (but not fully deficient) TLR signalling described for zymosan in the absence of TLR2 (ref. 12). In another approach, 293T cells transduced with GFP–LC3 and transiently transfected with TLR2 were cultured with zymosan (Supplementary Fig. 3c). Although phagocytosis by these cells is inefficient, phagosomes containing zymosan were observed to recruit GFP–LC3 only in those cells expressing TLR2. Thus, TLR signalling during phagocytosis induces a rapid recruitment of LC3 to the phagosome. However, we found that addition of the TLR ligands LPS or PAM3CSK4 to RAW cells that had engulfed latex beads did not induce recruitment of LC3 to the phagosomes at any time point (data not shown), suggesting that localized TLR signalling within the phagosome may be important for the recruitment process.

The formation of double-membrane structures and autophagosomes[8] were readily observed by electron microscopy of cells treated with rapamycin to induce autophagy or treatment with chloroquine to cause accumulation of autophagosomes[13] (Supplementary Fig. 4a). However, we failed to observe formation of such double-membrane structures associated with phagocytosed zymosan (Fig. 2a) despite recruitment of LC3. Pre-treatment of cells to induce autophagy (rapamycin or starvation) or the accumulation of autophagic vesicles (chloroquine) did not induce recruitment of LC3 to phagosomes in the absence of TLR signalling, or affect this recruitment in the presence of such signalling (Fig. 2b and Supplementary Fig. 5); furthermore, it did not cause the appearance of double-membrane structures associated with phagocytosed zymosan (Fig. 2a).

The autophagic vacuole has been suggested to derive from the endoplasmic reticulum (ER), based on localization of luminal ER proteins[14] and a requirement for Sec proteins in autophagosome formation[15]. In RAW cells treated with chloroquine, the dye ER-tracker co-localized with GFP–LC3 (Supplementary Fig. 4b and Supplementary Movie 3), representing autophagy of ER components[16] or a contribution of the ER to the autophagosome. No such co-localization was observed when cells engulfed zymosan, inducing GFP–LC3 association with the phagosome (Supplementary Fig. 4c and Supplementary Movie 4), again possibly distinguishing this phenomenon from autophagy.

Autophagosome formation requires a number of components of the autophagy pathway. Knockdown of ATG5 (Supplementary Fig. 6) markedly reduced the recruitment of GFP–LC3 to the zymosan-containing phagosomes (Fig. 3a, b). The role of the autophagy

[1]Department of Immunology, [2]Department of Tumor Cell Biology, and [3]Department of Biochemistry, St Jude Children's Research Institute, Memphis, Tennessee 38105, USA. [4]Laboratory of Frontier Science, Tokyo Metropolitan Institute of Medical Science, Bunkyo-ku, Tokyo 113-8613, Japan. [5]Department of Cancer Biology, The Scripps Research Institute, Jupiter, Florida 33458, USA.

pathway was further tested using macrophages derived from wild-type versus $Atg7^{-/-}$ mice. Whereas primary macrophages displayed association of GFP–LC3 with the phagosome after uptake of zymosan, no such association was observed in ATG7-deficient cells (Fig. 3c, d).

The initiation of the autophagy pathway involves members of the phosphoinositide-3-OH kinase (PI(3)K) family[17]. TLRs can similarly activate PI(3)K[18]. Pharmacological inhibition of PI(3)K using wortmannin or LY294002 (LY29) inhibited GFP–LC3 translocation (Fig. 3e, quantified in Fig. 3f). Wortmannin was added approximately 10 min after zymosan internalization to minimize the effects on engulfment[19]. Because phagocytosis itself engages PI(3)K[20], we used a probe derived from a phosphatidylinositol trisphosphate

(PtdIns3P)-binding PX-domain of p40 (phox)[21] to examine the appearance of PtdIns3P on the phagosome with or without TLR signalling. Transient, low-level PtdIns3P was seen in the absence of TLR signalling, whereas more persistent, higher levels were observed with TLR signalling (Fig. 3g, Supplementary Fig. 7, and Supplementary Movie 5), beginning before association of GFP–LC3 (Fig. 3g, Supplementary Fig. 7 and Supplementary Movies 6 and 7).

Initiation of the autophagy pathway involves beclin 1 (BECN1) in a complex with the PI(3)K hVps34 (also known as PIK3C3; ref. 4). Although no association of GFP–BECN1 with phagosomes occurred with latex beads (Supplementary Movie 8), zymosan induced an almost instantaneous association of GFP–BECN1 (as soon as 1 min after internalization) with the phagosome (Fig. 3h and Supplementary Movie 9).

TLR signalling proceeds, in part, through the adaptor molecule MyD88 (ref. 22). We found, however, that the absence of MyD88 did not affect the ability of TLR signalling by zymosan (Supplementary Fig. 8a) or red fluorescent E. coli (Supplementary Fig. 8b) to induce
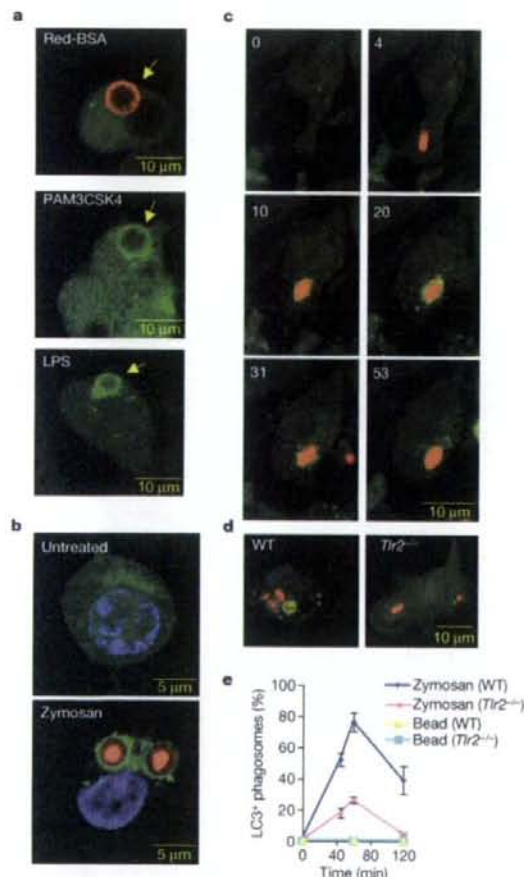

Figure 1 | TLR signalling activates components of the autophagy pathway. a, Internalization of beads with PAM3CSK, LPS, or Alexa-Fluor-555-labelled BSA (Red-BSA; yellow arrows) and association with GFP–LC3 in RAW cells was followed by time-lapse video for 3 h, 1 frame/2 min (representative frames are shown). **b,** GFP–LC3 in RAW cells translocates to phagosomes containing zymosan (red), assessed as in **a. c,** Time course of translocation of GFP–LC3 to a phagosome containing zymosan (red) (see Supplementary Movie 2). Time (minutes) is indicated in the top left of each panel. **d,** LC3 translocation to the phagosome is induced by TLR signalling. GFP–LC3 was transiently transfected into wild-type or $Tlr2^{-/-}$ macrophages, which were exposed to zymosan for 45 min. **e,** The percentage of phagosomes ($n \geq 50$ per group) with GFP–LC3 in wild-type and $Tlr2^{-/-}$ macrophages. Means and ranges are shown (4 mice per group were used).
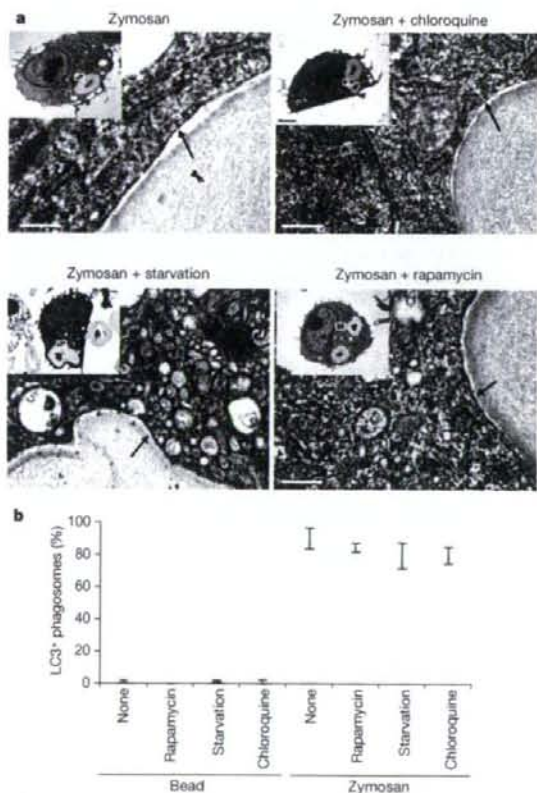

Figure 2 | TLR-induced LC3 localization to the phagosome appears to occur independently of autophagy. a, RAW-GFP–LC3 cells were treated with chloroquine (50 μM, 3 h) or rapamycin (200 nM, 6 h), or starved (6 h). Subsequently, the cells were exposed to zymosan for 1 h. We did not detect any double membranes associated with the phagocytosed zymosan (black arrows highlight single membranes) (scale bars equal 0.4 μm). **b,** RAW-GFP–LC3 cells were pre-treated with chloroquine (50 μM), starvation media, or rapamycin (200 nM) for 3 h. Cells were then fed with zymosan or beads and followed by time-lapse video at 3-min intervals for 3 h. All LC3-associated phagosomes ($n \geq 100$ per group) at all time points were quantified in three independent experiments (means and ranges are shown).

association of GFP–LC3 with the phagosome in primary macrophages. Pharmacological inhibition of p38, also implicated in TLR signalling[23], had a partial effect on translocation of GFP–LC3, reducing the frequency of associated phagosomes by about 30% (Supplementary Fig. 8c).

During phagocytosis of beads, limited fusion of the phagosomes with lysosomes (labelled with lysotracker red) was observed (Fig. 4a, b and Supplementary Movie 10). In contrast, beads coupled with the TLR ligand PAM3CSK4 induced a more rapid and extensive acidification (Fig. 4a, b, and Supplementary Movie 11). Similarly, phagosomes that had engulfed zymosan particles bound GFP–LC3 and then fused with lysosomes (Fig. 4c). This effect was inhibited by

knockdown of ATG5 (Fig. 4d). These results suggest that TLR-induced association of elements of the classical autophagy pathway to the phagosome promotes fusion with lysosomes.

At 4 h after phagocytosis, live *Saccharomyces cerevisiae* engulfed by ATG7-deficient macrophages showed a marked survival advantage over yeast taken up by wild-type macrophages (Fig. 4e). This strongly suggests that the TLR-induced recruitment of elements of the classical autophagy pathway to the phagosome has an impact on survival of engulfed organisms, especially at early time points. No differences in ATP levels in wild-type or $Atg7^{-/-}$ macrophages were detected (data not shown), and therefore the effects were not due to energetic defects in the null cells.
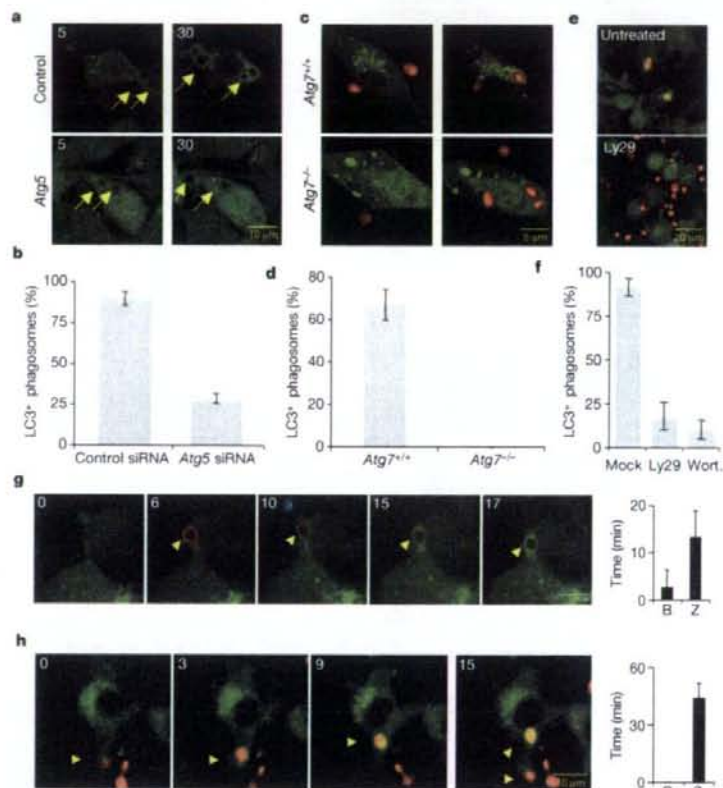

Figure 3 | Components of the autophagic pathway induce localization of LC3 to the phagosome on TLR stimulation. a, RAW cells expressing GFP–LC3 were transfected by electroporation with control or *Atg5* siRNA oligonucleotides. At 24 h after transfection, cells were fed with zymosan (yellow arrows) and the internalization process was followed by time-lapse video microscopy. Images obtained at 5 and 30 min after zymosan engulfment are shown. **b,** The percentage of GFP–LC3-associated phagosomes ($n \geq 100$ per /group) was obtained from three independent time-lapse videos (2 h each) of macrophages transfected with control or *Atg5* siRNA (means and ranges are shown). **c,** Bone-marrow-derived macrophages from wild-type and $Atg7^{-/-}$ mice were transiently transfected with GFP–LC3. After 24 h macrophages were fed with zymosan (red) for 1 h. Confocal images of the same cell before and after zymosan engulfment are shown. **d,** The percentage of GFP–LC3-associated phagosomes ($n \geq 50$ per group) was assessed after 1.5 h in wild-type and $Atg7^{-/-}$ macrophages (represented as means and ranges; three mice per group). **e,** Ly294002 (Ly29, 10 μM) was added 10 min before zymosan, and wortmannin was added after engulfment but before GFP–LC3 translocation in RAW-GFP-LC3 cells.

Representative images are shown. **f,** Percentage of GFP–LC3-associated phagosomes ($n \geq 50$ per group) with P(I)3K inhibitors assessed by time-lapse video (means and ranges are shown; three independent 3 h videos). **g,** RAW cells expressing GFP–LC3 and the PX domain of p40(phox) fused to mCherry (red) were fed with zymosan (yellow arrows) or with beads (Supplementary Fig. 6). Internalization was followed at 1-min intervals (Supplementary Movie 5), representative images are shown. Single cells were followed for at least 2 h ($n \geq 20$ per group) (Supplementary Movies 6, 7 and Supplementary Fig. 6). Mean ± s.d. duration of mCherry-PX translocation to the phagosome for beads (B) and zymosan (Z) are shown. **h,** Internalization of zymosan (yellow arrows) was followed at 1.5-min intervals for at least 2 h in RAW cells transiently transfected with GFP–BECN1. Representative images are shown. Translocation of GFP–BECN1 to the phagosome for beads (B) and zymosan (Z) was quantified (mean ± s.d.) using time-lapse movies (Supplementary Movie 8 and 9; $n \geq 20$ cells per group). For **g** and **h**, time (in minutes) is indicated at the top left of each panel.

Several recent studies have implicated autophagy in the removal of pathogens located in phagosomes, including *Mycobacterium tuberculosis*[3] and *Toxoplasma gondii*[24], as well as those that invade the cytosol, such as *Shigella flexneri*[25] and group A *Streptococcus*[2].
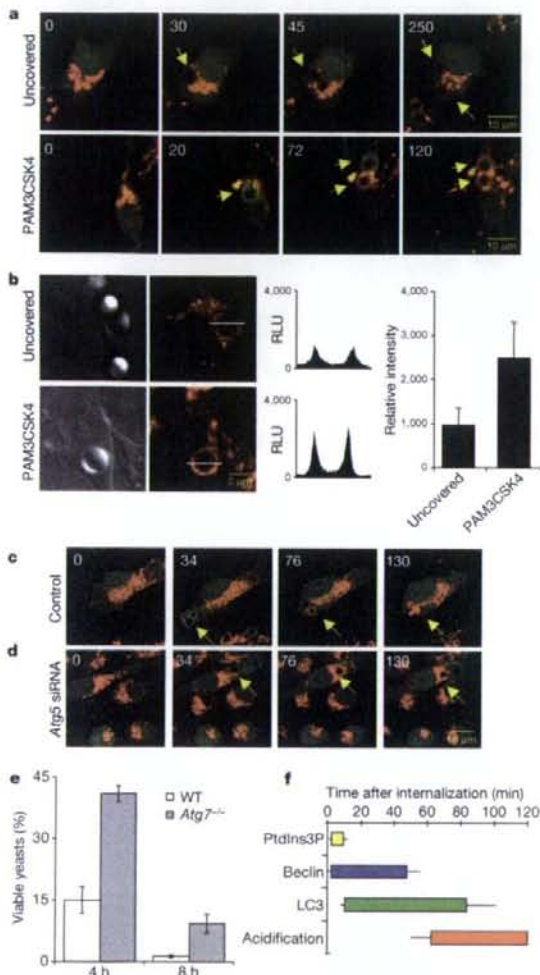

Figure 4 | TLR signalling induces phagosome maturation using components of the autophagic pathway. a, Internalization of control or PAM3CSK4-covered beads was followed in RAW-GFP–LC3 cells pre-loaded with lysotracker (red) by time-lapse video for 3 h. Time (in minutes) is indicated at the top left of each panel. **b**, RAW cells pre-loaded with lysotracker were exposed to control or PAM3CSK-covered beads for 6 h. Acidification of the beads ($n \geq 20$ per group), measured as maximum lysotracker relative light units (RLU) on a horizontal cross-section of each bead represented in the *x* axis (mean ± s.d.; Wilcoxon–Mann–Whitney test, $P < 0.0005$), is shown. **c, d**, Knockdown of ATG5 reduced zymosan-induced GFP–LC3 translocation and lysosomal fusion. **e**, Primary macrophages from wild-type (white bars) and *Atg7*-null mice (grey bars) were fed live yeast for 1 h and washed. Internalized yeast were extracted from the macrophages at 4 h and 8 h after re-plating. Means and ranges from six different measurements using two mice per group are shown. **f**, Initiation and duration of translocation of PX-mCherry to phagosomes (yellow bar), GFP–BECN1 translocation (blue bar), GFP–LC3 translocation (green bar) and Lysotracker recruitment (acidification) were determined during the first 2 h after internalization (10 cells per group, error bars indicate s.d.).

Autophagosomes either enclose the pathogens or fuse with the phagosome, and in at least one case this promotes phagosome maturation[24].

A recent publication[7] shows that engagement of TLR4 enhances conventional autophagy and autophagy directed to infectious organisms in the cytosol. We have found, in contrast, that TLR signalling during phagocytosis of an extracellular organism usurps the autophagy pathway to associate LC3 rapidly with the phagosome, apparently without the formation of conventional autophagosomes in this time period. We cannot, however, formally exclude that the association of LC3 with the phagosome is due to widespread and extremely rapid formation of small autophagosomes that fuse with the phagosome. Alternatively, vesicles derived from the secretory pathway and associated with elements of the autophagy pathway (including LC3) may dock, flatten and fuse with the phagosome, as described for phagosomes containing *Legionella*[26,27]. However, we were unable to observe this by either electron microscopy or in live cell imaging, even when autophagosomes were increased in the cells by rapamycin treatment or starvation to induce autophagy, or through the inhibitory action of chloroquine. Furthermore, the extremely rapid association of the phagosome with BECN1 (approximately 1 min) and a strong PI(3)K activity, followed by association with LC3 only a few minutes later, suggests the possibility that elements of the classical autophagy pathway are effectively and efficiently recruited to the phagosome on TLR signalling.

Although some studies[6,28] have shown that TLR signalling by means of MyD88 can enhance phagosome acidification and function, another study showed no effect of TLR signalling after engulfment of opsonized particles[29,30]. Here, we did not find a requisite role for MyD88 in the induction of translocation of LC3 to the phagosome, but found that engaging the autophagy pathway via TLR signalling enhanced phagosome maturation and destruction of the engulfed yeast.

METHODS SUMMARY

Mice and cells. All mice were bred and housed pathogen-free in our facility. Mouse primary macrophages were differentiated from fetal liver or from bone marrow and transiently transfected with GFP–LC3. RAW cells were stably transfected with GFP–LC3 (RAW-GFP–LC3) with or without PX-mCherry (RAW-LC3/Px), or transiently with BECN1–GFP.

Phagocytosis. Beads used for internalization were prepared by conjugating Alexa-Fluor-555-labelled BSA (Invitrogen) (Red-BSA) or PAM3CSK4 (Invivogen) to 6-μm diameter latex microspheres. Sonicated biotinylated-LPS (0.5 mg ml^{-1}) (Invivogen) was conjugated to SPHERO Streptavidin-polystyrene beads (Lybertiville). Zymosan particles were added at a ratio of 8:1 (particle:cell), whereas beads were added at a ratio of 10:1 (bead:cell). At the end of each experiment, we confirmed that particles were completely internalized by differential focusing.

Cell imaging. Two systems were used for live cell imaging: Marianas spinning-disk confocal imaging system (Intelligent Imaging Innovations/3i) and laser scanning confocal microscopy using a C1Si confocal system (Nikon). Laser scanning confocal microscopy on fixed tissues was performed with a Zeiss Axioplan 2 upright microscope equipped with an LSM 510 NLO confocal system (Carl Zeiss MicroImaging). For time-lapse microscopic imaging of phagocytosis, macrophages were plated on collagen-coated glass-bottom dishes (MatTek). Translocation of probes to the phagosome was quantified in time lapse movies.

1. Levine, B. Eating oneself and uninvited guests: autophagy-related pathways in cellular defense. *Cell* **120**, 159–162 (2005).
2. Nakagawa, I. et al. Autophagy defends cells against invading group A *Streptococcus. Science* **306**, 1037–1040 (2004).
3. Singh, S. B., Davis, A. S., Taylor, G. A. & Deretic, V. Human IRGM induces autophagy to eliminate intracellular mycobacteria. *Science* **313**, 1438–1441 (2006).
4. Levine, B. & Deretic, V. Unveiling the roles of autophagy in innate and adaptive immunity. *Nature Rev. Immunol.* **7**, 767–777 (2007).
5. Takeuchi, O. & Akira, S. Signaling pathways activated by microorganisms. *Curr. Opin. Cell Biol.* **19**, 185–191 (2007).

6. Blander, J. M. & Medzhitov, R. Regulation of phagosome maturation by signals from toll-like receptors. *Science* **304**, 1014–1018 (2004).

7. Xu, Y. *et al.* Toll-like receptor 4 is a sensor for autophagy associated with innate immunity. *Immunity* **27**, 135–144 (2007).

8. Tanida, I., Ueno, T. & Kominami, E. LC3 conjugation system in mammalian autophagy. *Int. J. Biochem. Cell Biol.* **36**, 2503–2518 (2004).

9. Mizushima, N., Yamamoto, A., Matsui, M., Yoshimori, T. & Ohsumi, Y. *In vivo* analysis of autophagy in response to nutrient starvation using transgenic mice expressing a fluorescent autophagosome marker. *Mol. Biol. Cell* **15**, 1101–1111 (2004).

10. Ozinsky, A. *et al.* The repertoire for pattern recognition of pathogens by the innate immune system is defined by cooperation between toll-like receptors. *Proc. Natl Acad. Sci. USA* **97**, 13766–13771 (2000).

11. Wooten, R. M. *et al.* Toll-like receptor 2 is required for innate, but not acquired, host defense to *Borrelia burgdorferi*. *J. Immunol.* **168**, 348–355 (2002).

12. Brown, G. D. *et al.* Dectin-1 is a major beta-glucan receptor on macrophages. *J. Exp. Med.* **196**, 407–412 (2002).

13. Schmid, D., Pypaert, M. & Munz, C. Antigen-loading compartments for major histocompatibility complex class II molecules continuously receive input from autophagosomes. *Immunity* **26**, 79–92 (2007).

14. Dunn, W. A. Jr. Studies on the mechanisms of autophagy: formation of the autophagic vacuole. *J. Cell Biol.* **110**, 1923–1933 (1990).

15. Ishihara, N. *et al.* Autophagosome requires specific early Sec proteins for its formation and NSF/SNARE for vacuolar fusion. *Mol. Biol. Cell* **12**, 3690–3702 (2001).

16. Bernales, S., Schuck, S. & Walter, P. ER-Phagy: selective autophagy of the endoplasmic reticulum. *Autophagy* **3**, 285–287 (2007).

17. Yorimitsu, T. & Klionsky, D. J. Autophagy: molecular machinery for self-eating. *Cell Death Differ.* **12** (suppl. 2), 1542–1552 (2005).

18. Kuo, C. C., Lin, W. T., Liang, C. M. & Liang, S. M. Class I and III phosphatidylinositol 3′-kinase play distinct roles in TLR signaling pathway. *J. Immunol.* **176**, 5943–5949 (2006).

19. Gillooly, D. J., Simonsen, A. & Stenmark, H. Phosphoinositides and phagocytosis. *J. Cell Biol.* **155**, 15–17 (2001).

20. Leverrier, Y. *et al.* Class I phosphoinositide 3-kinase p110β is required for apoptotic cell and Fcγ receptor-mediated phagocytosis by macrophages. *J. Biol. Chem.* **278**, 38437–38442 (2003).

21. Kanai, F. *et al.* The PX domains of p47phox and p40phox bind to lipid products of PI(3)K. *Nature Cell Biol.* **3**, 675–678 (2001).

22. Janssens, S. & Beyaert, R. A universal role for MyD88 in TLR/IL-1R-mediated signaling. *Trends Biochem. Sci.* **27**, 474–482 (2002).

23. Vasselon, T., Hanlon, W. A., Wright, S. D. & Detmers, P. A. Toll-like receptor 2 (TLR2) mediates activation of stress-activated MAP kinase p38. *J. Leukoc. Biol.* **71**, 503–510 (2002).

24. Andrade, R. M., Wessendarp, M., Gubbels, M. J., Striepen, B. & Subauste, C. S. CD40 induces macrophage anti-*Toxoplasma gondii* activity by triggering autophagy-dependent fusion of pathogen-containing vacuoles and lysosomes. *J. Clin. Invest.* **116**, 2366–2377 (2006).

25. Ogawa, M. *et al.* Escape of intracellular *Shigella* from autophagy. *Science* **307**, 727–731 (2005).

26. Amer, A. O. & Swanson, M. S. Autophagy is an immediate macrophage response to *Legionella pneumophila*. *Cell. Microbiol.* **7**, 765–778 (2005).

27. Tilney, L. G., Harb, O. S., Connelly, P. S., Robinson, C. G. & Roy, C. R. How the parasitic bacterium *Legionella pneumophila* modifies its phagosome and transforms it into rough ER: implications for conversion of plasma membrane to the ER membrane. *J. Cell Sci.* **114**, 4637–4650 (2001).

28. Blander, J. M. & Medzhitov, R. Reply to "Toll-like receptors and phagosome maturation". *Nature Immunol.* **8**, 217–218, doi:10.1038/ni0307-217b (2007).

29. Yates, R. M. & Russell, D. G. Phagosome maturation proceeds independently of stimulation of toll-like receptors 2 and 4. *Immunity* **23**, 409–417 (2005).

30. Russell, D. G. & Yates, R. M. Toll-like receptors and phagosome maturation. *Nature Immunol.* **8**, 217, doi:10.1038/ni0307-217a (2007).

A Neural-specific F-box Protein Fbs1 Functions as a Chaperone Suppressing Glycoprotein Aggregation*

Yukiko Yoshida[‡§1], Arisa Murakami[‡§], Kazuhiro Iwai[¶¶], and Keiji Tanaka[‡]

From the [‡]Tokyo Metropolitan Institute of Medical Science, 3-18-22 Honkomagome, Bunkyo-ku, Tokyo 113-8613, [§]CREST, Japan Science and Technology Corporation (JST), Saitama 332-0012, and the [¶]Department of Molecular Cell Biology, Graduate School of Medicine, Osaka City University, 1-4-3 Asahi-cyo, Abeno-ku, Osaka 545-8585, Japan

Fbs1 is an F-box protein present abundantly in the nervous system. Similar to the ubiquitously expressed Fbs2, Fbs1 recognizes N-glycans at the innermost position as a signal for unfolded glycoproteins, probably in the endoplasmic reticulum-associated degradation pathway. Here, we show that the *in vivo* majority of Fbs1 is present as Fbs1-Skp1 heterodimers or Fbs1 monomers but not SCF^{Fbs1} complex. The inefficient SCF complex formation of Fbs1 and the restricted presence of SCF^{Fbs1} bound on the endoplasmic reticulum membrane were due to the short linker sequence between the F-box domain and the sugar-binding domain. *In vitro*, Fbs1 prevented the aggregation of the glycoprotein through the N-terminal unique sequence of Fbs1. Our results suggest that Fbs1 assists clearance of aberrant glycoproteins in neuronal cells by suppressing aggregates formation, independent of ubiquitin ligase activity, and thus functions as a unique chaperone for those proteins.

The SCF (Skp1/Cul1/F-box protein) complex, the largest known class of sophisticated E3[2] ubiquitin ligases, consists of common components, Skp1, Cul1, and Roc1/Rbx1, as well as variable components known as F-box proteins that bind the substrates (1, 2). In this complex, the scaffold protein Cul1 (alias cullin1) interacts at the N terminus with the adaptor subunit Skp1 and at the C terminus with the RING-finger protein Roc1/Rbx1 that recruits a specific ubiquitin-activating enzyme (E2) for ubiquitylation. F-box proteins, interacting with Skp1 through the ~40 amino acid F-box motif, play an indispensable role in the selection of target proteins for degradation because each distinct F-box protein usually binds a protein substrate(s) with a degree of selectivity for ubiquitylation through C-terminal protein-protein interaction domains (3). The human genome contains 69 genes for F-box proteins and a large number of F-box proteins function in the specific ubiquitylation of a wide range of substrates. The F-box proteins are divided into three classes according to the type of substrate-binding domains. The two classes of binding domains are WD40

repeats and leucine-rich repeats, which are named Fbw (or FBXW) and Fbl (or FBXL) families, respectively (4). The third class of F-box proteins is the Fbx (or FBXO) family that does not contain any of these domains.

It has been reported that a subfamily under the Fbx family consists of at least five homologous F-box proteins containing a conserved FBA motif (5, 6). Among them, Fbs1/Fbx2/NFB42/Fbg1 and Fbs2/Fbx6b/Fbg2 can bind to proteins with high mannose oligosaccharides modification that occurs in the endoplasmic reticulum (ER) (7). Experiments using a fully reconstituted system showed that both Fbs1 and Fbs2 can form SCF-type ubiquitin ligase complexes specific for N-linked glycoproteins (7, 8). Overexpression of the Fbs1 or Fbs2 dominant-negative form or decrease of endogenous Fbs2 by small interfering RNA resulted in inhibition of degradation of endoplasmic reticulum-associated degradation (ERAD) substrates, suggesting the involvement of SCF^{Fbs1} and SCF^{Fbs2} in the ERAD pathway. Interestingly, x-ray crystallographic and NMR studies of the substrate-binding domain of Fbs1 have revealed that Fbs1 interacts with the innermost chitobiose in N-glycans of glycoproteins by a small hydrophobic pocket located at the top of the β-sandwich, indicating that both Fbs1 and Fbs2 efficiently recognize the inner chitobiose structure in Man$_{3-9}$GlcNAc$_2$ glycans (9). Indeed, the introduction of point mutation into the residues in the pocket impaired the binding activity toward its glycoprotein substrates. In general, the internal chitobiose structure of N-glycans in many native glycoproteins is not accessible by macromolecules. Fbs1 interacted with denatured glycoproteins more efficiently than native proteins, indicating that the innermost position of N-glycans becomes exposed upon protein denaturation and used as a signal of unfolded glycoproteins to be recognized by Fbs1 (10).

Of the Fbs family proteins, whereas Fbs2 is distributed ubiquitously in a variety of cells and tissues, Fbs1 is expressed only in neurons (7). In considering the involvement of these F-box proteins in the ERAD pathway in general, the restricted expression of Fbs1 in neurons remains a mystery. In this study, we found that the major population of Fbs1 protein did not form the SCF^{Fbs1} complex in cells although Fbs1 is known to act as a compartment of SCF-type ubiquitin ligase (8). Moreover, the results showed that the sequence of the intervening segment between the F-box domain and the substrate-binding domain of the Fbs1 hampered the assembly of the SCF^{Fbs1} complex in the cytosol without affecting the association with Skp1. The Skp1-Fbs1 heterodimers as well as SCF^{Fbs1} complex effectively prevented the aggregation of the glycoprotein *in vitro*, and this

- 392 -

activity was dependent on the presence of the N-terminal domain and the substrate-binding domain of Fbs1. Our data thus imply that Skp1 and Fbs1 may function in both SCF and non-SCF complexes.

EXPERIMENTAL PROCEDURES

Affinity Purification and Immunoprecipitation of Brain Lysate—The preparation of lysates from mouse brains and purification of Fbs1 by using a ribonuclease B (RNaseB) column were performed as described previously (10). For immunoprecipitation, we used polyclonal antibody to Fbs1 as described previously (11). For immunoblotting, we used rabbit polyclonal antibodies against Fbs1, Cul1 (Zymed Laboratories Inc., San Francisco, CA) and Skp1 (Santa Cruz Biotechnology, Santa Cruz, CA), and horseradish peroxidase-conjugated goat anti-rabbit IgG (Jackson ImmunoResearch Laboratories, West Grove, PA) for Fbs1 and Skp1 blots or horseradish peroxidase-conjugated goat anti-rabbit IgG light chain (Jackson ImmunoResearch Laboratories) for Cul1 blots. Lectin blotting was performed by using horseradish peroxidase-conjugated ConA (Seikagaku-kogyo, Japan) as described previously (11).

Glycerol Gradient Analysis—The fraction eluted with 0.1 M chitobiose from the RNaseB resin was prepared from 0.5 ml of lysates (14 mg/ml) from mouse brains. The eluate was dialyzed against TBS. The resultant fraction and a 1-mg lysate of brains were used for glycerol gradient analysis. Samples and molecular weight markers (Amersham Biosciences) were fractionated by 4–17% (v/v) linear glycerol density gradient centrifugation (22 h, $100,000 \times g$) as described previously (12).

Cell Culture and Immunological Analysis—PC12 cells were grown in RPMI medium 1640 (Invitrogen) supplemented with 10% horse serum and 5% fetal bovine serum. For neuronal differentiation, PC12 cells were treated with 10–20 ng/ml nerve growth factor (Invitrogen) on collagen-coated plates. 293T and HeLa cells were grown in Dulbecco's modified Eagle's medium (Sigma) supplemented with 10% fetal bovine serum and were transfected as described previously (8). FLAG-tagged Fbs1 mutant vectors consisting of Fbs1 and Fbs2 fragments were generated by PCR, and those sequences were verified. Whole cell lysates were prepared with 20 mM Tris-HCl (pH 7.5), 150 mM NaCl (TBS) containing 0.5% Nonidet P-40. The supernatant and precipitate fractions were prepared by ultracentrifugation of the supernatant that was prepared by centrifugation of freezing-and-thawing cell lysates in TBS at $8,000 \times g$ for 20 min and at $100,000 \times g$ for 60 min. The precipitate fraction was solubilized with Triton X-100. Each immunoprecipitation analysis was performed for whole cell lysates or subcellular fraction of cells by using the same amount of proteins. Monoclonal antibodies to calnexin and rhodopsin were purchased from BD Transduction Laboratories and Affinity Bioreagents (Golden, CO), respectively. Antibodies to FLAG, HA, and fetuin have been described previously (8).

Pulse-chase Analysis—The expression plasmid for P23H rhodopsin was kindly provided by M. E. Cheetham (University College London). Pulse-chase experiments were performed as described previously (7). Briefly, 293T cells were transfected with 1 μg of P23H rhodopsin expression plasmid and 1 μg of FLAG-tagged Fbs1 derivatives or pcDNA3-FLAG plasmid.

Twenty-four hours after transfection, the cells were starved for 30 min and labeled for 1 h with 150 μCi of Pro-Mix L-^{35}S *in vitro* cell labeling mix (Amersham Biosciences) per milliliter. After washing, the cells were chased with complete Dulbecco's modified Eagle's medium supplemented with fetal bovine serum in the presence or in the absence of 50 μg/ml MG132 (Peptide Institute, Tokyo, Japan) for the indicated time intervals. After the harvested cells were lysed by TBS containing 0.1% SDS and 1% Nonidet P-40, immunoprecipitation was performed with anti-rhodopsin and FLAG antibodies.

Preparation of Recombinant Proteins and in Vitro Ubiquitylation Assay—The His-tagged Fbs1 ΔF, Fbs1 ΔP baculovirus were produced by Bac-to-Bac baculovirus expression system (Invitrogen). The SCF^{Fbs1}, Skp1-Fbs1 dimers, Fbs1 Fbs1 ΔF, Fbs1 ΔP, Skp1-ΔP dimers, and Fbs1 ΔN were obtained by baculovirus-infected HighFive cells as described previously (10). These proteins were purified by affinity chromatography using RNaseB-immobilized beads as a ligand and chitobiose as an eluent, and the eluates were dialyzed to 1,000 volumes of TBS three times. *In vitro* ubiquitylation assays were performed as described previously (10).

Aggregation Assay—Jack bean α-mannosidase (Sigma) was desalted using a NAP-25 gel filtration column (Amersham Biosciences) equilibrated in 10 mM Tris-HCl (pH 8.0). The desalted protein was lyophilized and redissolved at 21.7 μM in 0.1 M Tris-HCl (pH 8.0) and 6 M GdnHCl as described previously (13). After denaturation for 60 min at room temperature, samples were diluted to 0.3 μM in 1 ml of TBS containing various concentrations of bovine serum albumin or recombinant Fbs1 derivatives. Protein aggregation was monitored at 25 °C over a period of 60 min by measuring absorbance at 360 nm.

RESULTS

Multiple States of Fbs1 in Brain—Fbs1 has been found in the fraction eluted with di-*N*-acetyl-D-glucosamine (thereafter referred to as chitobiose) from GlcNAc-terminated fetuin of lysates prepared from mouse brain (8). Fbs1 and Skp1 proteins were detected in the eluted fraction with Coomassie Brilliant Blue staining, but we could not detect the apparent band of Cul1. However, the formation of the SCF^{Fbs1} complex was confirmed not only by reciprocal immunoprecipitation experiments in 293T cells but also by reconstitution of baculovirally expressed recombinant SCF^{Fbs1} proteins. To address these contradictory observations, we tested whether endogenous Fbs1 in the mouse brain forms the SCF complex by examining the interaction of Fbs1 with Cul1 (Fig. 1A). Fbs1 can be easily purified by affinity chromatography using RNaseB that contains a high mannose oligosaccharide as a ligand and chitobiose as an eluent (10). Since Fbs1 contains a single binding domain toward an *N*-glycan, it seems likely that the eluted Fbs1 protein or its complex from the RNaseB-immobilized resin is free from its substrates. Indeed, the glycoproteins modified with high mannose oligosaccharides were not included in the eluates by chitobiose (Fig. 1B). Although Skp1 was effectively co-immunoprecipitated with Fbs1 from the lysate of mouse brain, the amount of Skp1 that was eluted with Fbs1 from the RNaseB resin was small (Fig. 1A). Despite the difference in the quantities of Skp1 bound to Fbs1 in the fractions between eluates from
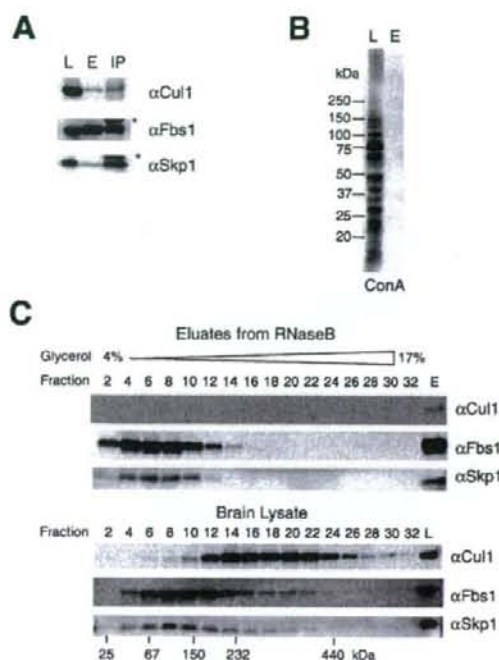
- 393 -

FIGURE 1. **States of Fbs1 in mouse brain.** *A*, 0.6 mg of lysate from adult mouse brain was subjected to RNaseB-immobilized affinity column and eluated with chitobiose (*E*) or subjected to immunoprecipitation with an antibody to Fbs1 (*IP*). Thirty μg of lysate (*L*), one-tenth of eluate, and immunoprecipitate were analyzed by immunoblotting with antibodies to Cul1, Fbs1, or Skp1. *Asterisks* show Ig heavy chain (*αFbs1*) and light chain (*αSkp1*). *B*, ConA lectin blot for brain lysate (*L*) and the eluate from the RNaseB resin (*E*) against the same amounts of proteins described in *A*. *C*, adult mouse brain lysate (*lower panel*, 0.7 mg) and lysate eluated with chitobiose from RNaseB (*upper panel*, started from 7 mg of the lysate) were separated by 4–17% glycerol density gradient centrifugation. One-third of each fraction was analyzed by immunoblotting with antibodies to Cul1, Fbs1, and Skp1. *Molecular size markers* are indicated below.

the RNaseB resin and immunoprecipitation with an anti-Fbs1 antibody, almost the same and small quantities of Cul1 were detected in these fractions. These results suggest that major populations of substrate-free Fbs1 and substrate-binding Fbs1 are present as Fbs1 monomers and Fbs1-Skp1 dimers, respectively, and the binding of substrates to Fbs1 does not influence the weak SCF complex formation.

To examine the behavior of endogenous Fbs1 in more detail, eluates from the RNaseB resin and lysates from the mouse brain were separated by a 4–17% glycerol density gradient centrifugation (Fig. 1*C*). The distribution of Fbs1 (~42 kDa) in the chitobiose eluates corresponded to the position of Fbs1 monomers (fraction 4) and Skp1-Fbs1 dimers (~63 kDa)(fraction 6). Although Cul1 was not detected in any fractions, the peak of Skp1 in eluates from the RNaseB resin was in the position of the Skp1-Fbs1 dimer. On the other hand, Fbs1 protein in brain lysate was detected in a broad range of fractions mainly larger than Fbs1-Skp1 dimers, indicating that most Fbs1, if not all, is associated with various glycoprotein substrates; *i.e.* Fbs1-Skp1 dimers maintain the association with glycoproteins *in vivo*. Cul1 (~90 kDa) in brain lysate was distributed broadly in

higher density fractions, indicating its association with various other SCF-components.

Minor Population of Fbs1 Forms SCF Complex on ER—We next expressed FLAG-tagged F-box proteins alone or their combination with HA-tagged Skp1 in 293T cells and immunoprecipitated with anti-FLAG and anti-HA antibodies (Fig. 2*A*). The expression of HA-tagged Skp1 increased the amount of exogenous F-box proteins, suggesting that Skp1 stabilizes F-box proteins (*lanes 1–8*). Cul1 was co-immunoprecipitated with Fbs2 and Fbg3, which are highly homologous with Fbs1, or βTrCP1/Fbw1, one of the Fbw family members (*lanes 11–16*). The interaction between Cul1 and these F-box proteins increased upon co-expression of Skp1. However, unlike these F-box proteins, Fbs1 was almost undetectable in the immune complex with Cul1, regardless of the overexpression of exogenous Skp1 (*lanes 9* and *10*), although Fbs1 was co-immunoprecipitated with Skp1 as well as other F-box proteins (*lanes 18, 20, 22*, and *24* in the *αFlag panel*). Moreover, the amount of Cul1 associated with exogenous Skp1 was lower in the presence of Fbs1 than in those of other F-box proteins, suggesting that expression of Fbs1 prevents forming other SCF complexes by dimerizing with Skp1 (*lanes 18, 20, 22*, and *24* in the *αCul1 panel*). These results suggest that Fbs1 can strongly bind Skp1 but is weak in forming the SCF[Fbs1] complex.

We have recently reported that Fbs1 is a cytosolic protein but that part of Fbs1 associates with the ER membrane through interaction with p97/VCP (valosin-containing protein) (11). We next examined whether the ER membrane-associated Fbs1 formed the SCF complex. Lysates of 293T and HeLa cells expressing FLAG-tagged Fbs1 were fractionated into the $100,000 \times g$ supernatant and precipitate fractions excluding the $8,000 \times g$ precipitate, and then Fbs1 was immunoprecipitated from these fractions by anti-FLAG antibody. As shown in Fig. 2*B*, Cul1 was co-immunoprecipitated with Fbs1 mainly from the precipitate (*p*) fraction (*lanes 4* and *8*). Although the association of Fbs1 with Skp1 occurred more effectively in the supernatant (*s*) fraction, the formation of the SCF complex, including Fbs1, was hardly detected in the supernatant fraction (*lanes 3* and *7*). Moreover, we examined whether endogenous Fbs1 formed the SCF complex in the precipitate fraction using nerve growth factor-treated PC12 cells, which endogenously express Fbs1 (14). As shown in Fig. 2*C*, part of Cul1 was co-immunoprecipitated with Fbs1 from the precipitate (*p*) fraction. These results indicate that the major population of endogenous Fbs1 is present as the Fbs1-Skp1 heterodimers or the Fbs1 monomers in the cytosol, and a minor population of Fbs1 forms the SCF complex bound on the ER membrane.

Linker Sequence of Fbs1 Prevents SCF Complex Formation—Although the SCF complex formation of Fbs1 was inefficient, Fbs2 formed the SCF complex effectively (Fig. 2*A*). To identify the region(s) of Fbs1 that impedes SCF complex formation, we examined the ability of various fusion proteins containing Fbs1 and Fbs2 fragments to form the complex and compared these findings with the full-length proteins in co-immunoprecipitation assay (Fig. 3*A*). Fbs1 ΔF was used as negative control that did not bind to Skp1 (Fig. 3*B*, *lane 3*). Fbs1 YW and Fbs1 ΔC, both of which are deficient in substrate binding, could not restore SCF complex formation, indicating that the interaction
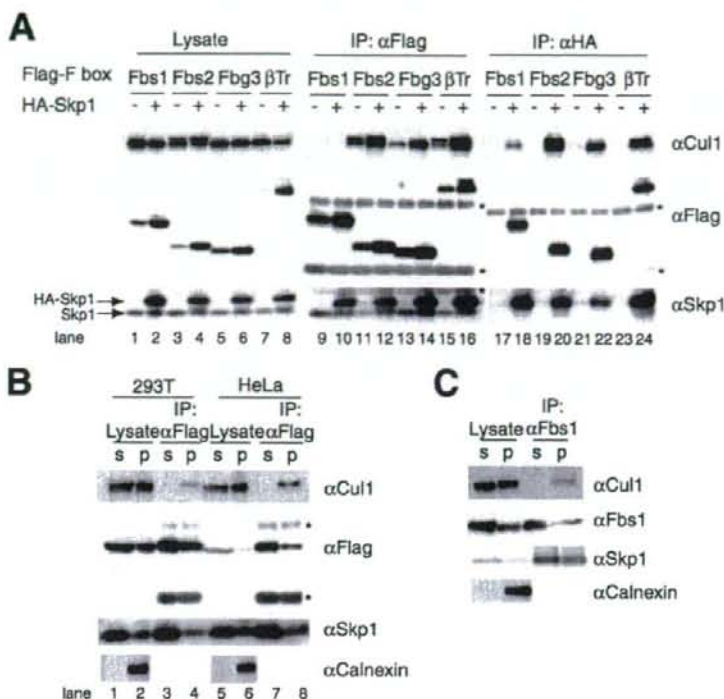
- 394 -

A

B **C**

FIGURE 2. **Major population of Fbs1 forms non-SCF complex in vivo.** *A*, 293T cells were transfected with plasmids encoding various FLAG-tagged F-box proteins (Fbs1, Fbs2, Fbg3, and βTrCP1 (*βTr*)) combination with empty HA plasmids (−) or plasmids encoding HA-tagged Skp1 (+). Whole cell lysates were subjected to immunoprecipitation (*IP*) with antibodies to FLAG and HA, and lysates (15 μg each) and one half of the resulting precipitates were analyzed by immunoblotting with antibodies to Cul1, FLAG, and Skp1. *Asterisks* show Ig heavy and light chains. *B*, 293T and HeLa cells were transfected with FLAG-tagged Fbs1. Cell lysates were fractionated by ultracentrifugation, and FLAG-Fbs1 was immunoprecipitated with an antibody to FLAG from the same amount of proteins of 100,000 × *g* supernatant (*s*) and precipitate (*p*) fractions. The total amount of protein of the supernatant fraction was 2–3 times larger than that of the precipitate fraction. Lysates (15 μg each) and immunoprecipitates were analyzed by immunoblotting with antibodies to Cul1, FLAG, and Skp1. *Asterisks* show Ig heavy and light chains. To control for the fractionation, immunoblotting with an antibody to calnexin was performed. *C*, endogenous Fbs1 was immunoprecipitated with an antibody to Fbs1 from 100,000 × *g* supernatant, and precipitate fractions of differentiated PC12 cells were treated with nerve growth factor. Lysates (15 μg each) and immunoprecipitates were analyzed by immunoblotting. The immunoblotting analysis for separated supernatant and precipitate fractions was conducted as for *B*.

between Fbs1 and its substrates does not affect the complex formation (*lanes 4* and *5*). The N-terminal sequence of Fbs1 called the P domain is unique and is not seen in other F-box proteins, but the removal of this domain from Fbs1 or the addition to Fbs2 did not affect the complex formation (Fbs1 ΔP and Fbs2 P1: *lanes 6* and *13*). Exchange of the F-box domains between Fbs1 and Fbs2 caused the loss of the Skp1 binding activity, probably due to the incorrect folding (Fbs1 F2, Fbs1 ΔPF2, Fbs2 F1, and Fbs2 PF1: *lanes 7, 8, 10,* and *11*, respectively). However, the replacement of the Fbs1 N-terminal region (which contains P and F-box domains and linker sequence) with the Fbs2 N-terminal region rescued the complex formation (Fbs-2N1C: *lane 9*). In contrast, the addition of the Fbs1 N-terminal region instead of the Fbs2 N-terminal region markedly reduced the activity of Fbs2 to form the SCF complex but did not affect the Skp1 binding (Fbs-1N2C: *lane 12*). The linker sequences of the intervening segments between the F-box domain and the substrate-binding domain showed

lower homology than other portions between Fbs1 and Fbs2, suggesting that the Fbs1 linker sequence is responsible for impeding the SCF^{Fbs1} complex formation. Indeed, only the Fbs1 mutant protein that contained the Fbs2 linker sequence could form the SCF complex, but the efficiency of the SCF complex formation was less than that of Fbs-2N1C (Fbs1 I2: *lane 15*). On the other hand, Fbs2 protein containing the Fbs1 linker sequence and the Fbs1 protein without its linker sequence did not seem to show the correct folding for Skp1 binding (Fbs2 I1 and Fbs1 ΔI: *lanes 16* and *17*). The Fbs1 mutant in which the F-box domain and the linker sequence are replaced with those of Fbs2 forms the SCF complex effectively. Thus, we conclude that the Fbs1 linker sequence between the F-box and substrate-binding domains hampers the SCF^{Fbs1} complex formation.

We next compared the localization of Fbs1, Fbs2, and the mutant Fbs1 proteins capable of forming the SCF complex: Fbs-2N1C and Fbs1 I2 (Fig. 3C). Although a minor population of Fbs1 in the precipitate (*p*) fraction formed the SCF complex, most Fbs2 formed the SCF^{Fbs2} complex in the supernatant (*s*) fraction as well as the precipitate fraction. Fbs-2N1C could form the SCF complex mainly in the supernatant fraction (Fig. 3C). Moreover, the amount of Cul1 co-immunoprecipitated with Fbs1 I2 was similar in both fractions. These results suggest that the linker sequence of Fbs1 does not only impede the formation of the SCF complex but also restricts the localization of the SCF complex bound on the ER membrane.

Expression of Mutant Fbs1 That Forms E3 Easily Induces Proteolysis of Its Substrates—To confirm that most Fbs1 in the cells is inactive to function as an E3 ubiquitin ligase, we next examined the ability of the mutant Fbs1 that readily forms the SCF complex (Fbs-2N1C) to ubiquitylate the substrates. It has been shown that P23H mutated rhodopsin (hereafter referred to as P23H) is an ERAD substrate, and its *N*-linked glycosylation is required for the degradation (15, 16). As reported previously, rhodopsin monomer is ~40–43 kDa, but the majority of P23H was detected as high molecular weight complex multimers by immunoblotting with anti-rhodopsin antibody (Fig. 4A). Wild-type Fbs1, but not the substrate-binding defective mutant Fbs1 YW, was able to associate with P23H effectively, suggesting that Fbs1 binds to P23H through its *N*-glycans. On the other hand,
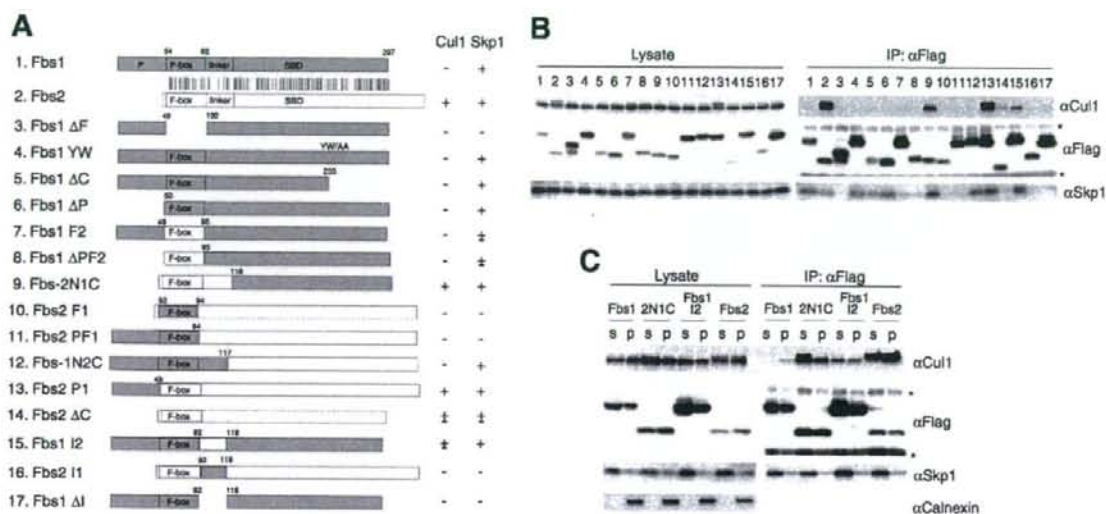
FIGURE 3. **Linker sequence between F-box and substrate-binding domains of Fbs1 hampers SCF^Fbs1 complex formation.** *A*, schematic representation of constructs of fusion proteins consisting of Fbs1 and Fbs2 fragments. The fragments derived from Fbs1 and Fbs2 appear in *gray* and *white boxes*, respectively. The *numbers* above the constructs represent the amino acid position of Fbs1. The *vertical bars* represent identical amino acids between Fbs1 and Fbs2. P and F-box domains, linker sequence, and sugar-binding domain are represented by *P*, *F-box, linker*, and *SBD*, respectively. The binding activities of these constructs toward Cul1 and Skp1 shown in *B* are summarized on the *right*, with + representing strong binding, ± representing weak binding, and − representing no binding. *B*, 293T cells were transfected with plasmids encoding the FLAG-tagged mutants F-box proteins represented in *A*. Whole cell lysates were subjected to immunoprecipitation (*IP*) with an antibody to FLAG, and the resulting precipitates were analyzed by immunoblotting with antibodies to Cul1, Skp1, and FLAG. *Asterisks* show Ig heavy and light chains. *C*, 293T cells were transfected with FLAG-tagged Fbs1, Fbs-2N1C, Fbs1 I2, or Fbs2. Cell lysates were fractionated by ultracentrifugation, and FLAG-Fbs1 was immunoprecipitated with an antibody to FLAG from 100,000 × *g* supernatant (*s*) and precipitate (*p*) fractions. The resulting immunoprecipitates were analyzed by immunoblotting as in Fig. 2*B*.
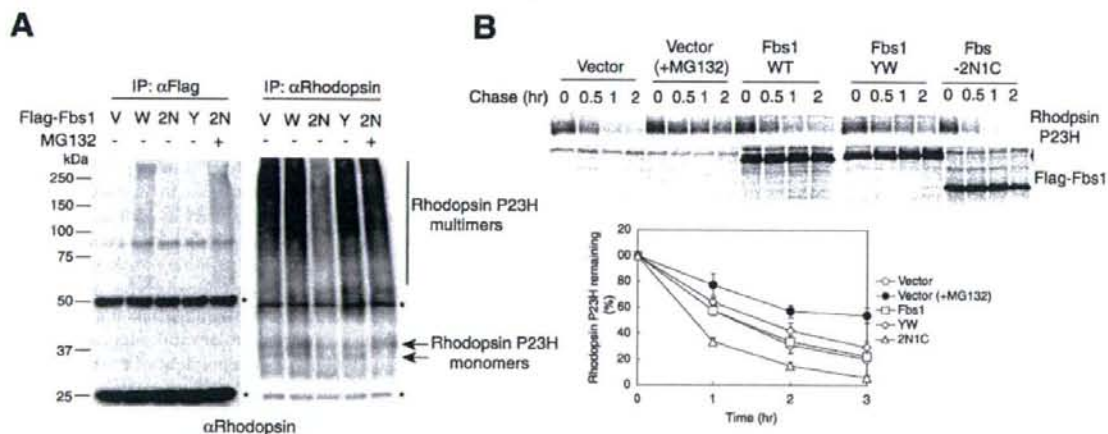

FIGURE 4. **Expression of Fbs-2N1C promotes substrate degradation.** *A*, 293T cells were transfected with plasmids encoding FLAG-tagged empty vector (*V*), Fbs1 (*W*), Fbs-2N1C (*2N*), or Fbs1 YW (*Y*) and combination with rhodopsin P23H mutant. Some cells were treated with 10 μM MG132 for 16 h. Whole cell lysates were subjected to immunoprecipitation (*IP*) with antibodies to FLAG and rhodopsin, and the resulting precipitates were analyzed by immunoblotting with an antibody to rhodopsin. *Asterisks* show Ig heavy and light chains. *B*, rhodopsin P23H was co-transfected with FLAG-tagged empty vector, Fbs1, Fbs-2N1C, or Fbs1 YW. Twenty-four hours after transfection, 293T cells were pulse-labeled with [³⁵S]Met/Cys for 1 h and chased for the indicated time intervals. Rhodopsin P23H and Fbs1 derivatives were immunoprecipitated with antibodies to rhodopsin and FLAG, respectively. The plotted data at the bottom show a quantification analysis of the stability of rhodopsin P23H over time in the *upper panels*. Data are the mean ± S.D. of three independent experiments. *WT*, wild type.

Fbs-2N1C could bind to P23H, although its binding to P23H seemed weaker than that of wild-type Fbs1 (Fig. 4*A*, *left panel*). Since the activity to bind RNaseB was not different between Fbs1 and Fbs-2N1C (data not shown), it seems likely that the SCF^Fbs-2N1C causes degradation of P23H through its ubiquitylation. Interestingly, the quantity of P23H decreased upon Fbs-

2N1C expression (Fig. 4*A, right panel*). It has been reported that the degradation of P23H was suppressed by MG132 treatment (15, 16). The quantities of both P23H associated with Fbs-2N1C and the P23H protein were recovered by the addition of MG132. Moreover, we performed pulse-chase analysis using 293T cells co-expressing the P23H mutant and FLAG-tagged